Geochemistry Geophysics Geosystems G3

Article
Volume 13, Number 1
XX Month 2012
QXXXXX, doi:10.1029/2011GC003843
ISSN: 1525-2027

Published by AGU and the Geochemical Society

Spherical dynamic models of top-down tectonics

G. Morra
School of Earth and Environmental Sciences, Seoul National University, Seoul 151-746, South Korea (gabrielemorra@gmail.com)

School of Geosciences, University of Sydney, Sydney, New South Wales 2006, Australia

L. Quevedo and R. D. Müller
School of Geosciences, University of Sydney, Sydney, New South Wales 2006, Australia

[1] We use the Multipole–Boundary Element Method (MP-BEM) to simulate regional and global geodynamics in a spherical 3-D setting. We first simulate an isolated subducting rectangular plate with length (L_{litho}) and width (W_{litho}) varying between 0.5 and 2 times the radius of the Earth (R_{Earth}) and with viscosity η_{litho} varying between 100 and 500 times the upper mantle (η_{UM}), sinking in a layered mantle characterized by lower-upper mantle viscosity ratio $\lambda = \eta_{LM}/\eta_{UM}$ varying between 1 and 80. In a mantle with small upper/lower viscosity contrast ($\lambda \cong 1$), trench and plate motions are weakly dependent on W_{litho}; plate motion is controlled by slab pull if $L_{litho} \leq R_{Earth}$, while for longer plates plate speed strongly decreases because of the plate basal friction and flow reorganization. An increasing viscosity ratio λ gradually breaks this pattern, and for $\lambda \cong 10$ combined with $W_{litho} \approx R_{Earth}$ (and greater) trench advance and retreat are simultaneously observed. These results offer a first-order explanation of the origin of the size ($L_{litho} \approx W_{litho} \approx R_{Earth}$) of the largest plates observed over the past 150 Myr. Finally, two global plate tectonic simulations are performed from reconstructed plates and slabs at 25 Ma before present and before 100 Ma, respectively. It is shown that MP-BEM predicts present plate kinematics if plate-mantle decoupling is adopted for the longest plates ($L_{litho} > R_{Earth}$). Models for 100 Ma show that the slab-slab interaction between India and Izanagi plates at 100 Ma can explain the propagation of the plate reorganization from the Indian to the Pacific plate.

Components: 16,700 words, 14 figures, 3 tables.

Keywords: Boundary Element Methods; global models; numerical models; plate tectonics; plates; subduction.

Index Terms: 3040 Marine Geology and Geophysics: Plate tectonics (8150, 8155, 8157, 8158); 8155 Tectonophysics: Plate motions: general (3040); 8157 Tectonophysics: Plate motions: past (3040).

Received 22 August 2011; **Revised** 19 January 2012; **Accepted** 19 January 2012; **Published** XX Month 2012.

Morra, G., L. Quevedo, and R. D. Müller (2012), Spherical dynamic models of top-down tectonics, *Geochem. Geophys. Geosyst.*, *13*, QXXXXX, doi:10.1029/2011GC003843.

1. Introduction

[2] One of the most striking phenomena that have arisen during the evolution of the Earth is the tessellation of its surface into lithospheric plates, whose largest ones have comparable size to mantle thickness [*Bird*, 2003]. Numerical models of mantle convection have shown that if a threshold to maximum stress is applied, the top stiff boundary layer self-consistently split in plates of sizes

10.1029/2011GC003843

comparable to the largest on the Earth [*Trompert and Hansen*, 1998; *Bercovici*, 1998; *Tackley*, 2000b]. Furthermore, convection models in which the mantle is heated from within show that the plate-mantle system organizes itself as a top-down process, where the forces propagates from the subducting slabs to the plates on the surface [*Buffett et al.*, 1994]. This scenario is in agreement with the classical view that the major driver of plate tectonics is the slab pull [*Forsyth and Uyeda*, 1975; *Lithgow-Bertelloni and Richards*, 1998]. However, the exact way the force is transmitted from the slab to the plate is still debated [*Becker and O'Connell*, 2001; *Conrad and Lithgow-Bertelloni*, 2002], with direct consequences on our understanding of plate stresses [*Lithgow-Bertelloni and Guynn*, 2004] and the causes of the largest earthquakes [*Buffett and Heuret*, 2011].

[3] Several factors have been put forward for affecting the transmission of the slab pull. Among these factors are the bending [*Conrad and Hager*, 1999; *Becker et al.*, 1999; *Capitanio et al.*, 2009] and tensile strength [*Regenauer-Lieb et al.*, 2006; *Morra et al.*, 2006; *Capitanio et al.*, 2007] of the lithosphere, plate boundary frictional forces [*Zhong and Gurnis*, 1995a; *Iaffaldano et al.*, 2006; *Capitanio et al.*, 2010; *van Dinther et al.*, 2010], the basal drag due to slab sinking [*Conrad and Hager*, 2001; *Lithgow-Bertelloni and Guynn*, 2004] and the mantle drag to the sinking plates themselves [*Faccenna et al.*, 1996; *Schellart et al.*, 2002; *Funiciello et al.*, 2003a], the interaction between slabs through mantle flow [*Loiselet et al.*, 2009; *King*, 2001; *Wu et al.*, 2008], and the dynamic topography of the earth surface, partially controlling trench kinematics [*Funiciello et al.*, 2003a; *Schmeling et al.*, 2008].

[4] Geodynamics at the regional scale (a subduction zone one or few thousands km long) has been investigated through with laboratory and numerical methods. Complexities have emerged from the investigation of the role of the internal deformation in the lithosphere [*Conrad and Hager*, 1999; *Regenauer-Lieb et al.*, 2001] versus the associated mantle flow [*Funiciello et al.*, 2003a; *Moresi and Gurnis*, 1996]. Recent numerical simulations have shown that the subducting lithosphere adapts its morphology following a principle of minimum dissipation at the trench [*Morra et al.*, 2006; *Capitanio et al.*, 2007, 2009; *Stadler et al.*, 2010; *Ribe*, 2010], although this result remains controversial [*Buffett and Rowley*, 2006; *Buffett and Heuret*, 2011; *Conrad and Hager*, 1999; *Di Giuseppe et al.*, 2008]. Low dissipation in the slab implies that the speed of the subduction process is only determined by the equilibrium between active forces (slab pull) and resisting forces (mantle drag) [*Faccenna et al.*, 2001; *Funiciello et al.*, 2003b]. Comparison with nature indicates that this scaling is substantially reflected by plate velocities in the Cenozoic [*Goes et al.*, 2008].

[5] Three-dimensional regional studies of subduction have led to the discovery of the major role played by plate width [*Morra et al.*, 2006], in particular when the trenches are several thousands km long [*Stegman et al.*, 2006]. This result has produced controversial interpretations of kinematic data, suggesting that not plate age (proportional to slab pull) but plate size (related to the drag due to mantle flow) might better fit kinematic data [*Schellart et al.*, 2008; *Stegman et al.*, 2010a]. While the small number of trenches and the ambiguity of the boundary of each subduction zone leave little space to a definitive interpretation of the present kinematic data, the comparison of regional and global models with plate reconstructions in the last 100 Myr offer a clearer insights on the role of other important parameters controlling plate tectonics, such as plate length and degree of mantle stratification.

[6] While this scenario explains many features of regional kinematics, how such effects influence global models is less understood. Early attempts to address this problem have used semi-analytical circulation models [*Hager and O'Connell*, 1981], followed by models in which plate geometry was prescribed and the mantle flow solution was used to calculate the torque at the base of the plates [*Ricard and Vigny*, 1989; *Lithgow-Bertelloni and Richards*, 1998]. Forces at the boundary of the plates were later introduced [*Becker and O'Connell*, 2001] and brought to the conclusion that one-sided subduction is an essential ingredient in order to explain the large difference between oceanic and continent plate motion [*Conrad and Lithgow-Bertelloni*, 2002], implying that the driver of plate motion is the presence of strong slabs able to transmit the pull. In the last years, the introduction in global models of lateral viscosity variations [*Zhong et al.*, 2000; *Tan et al.*, 2006], suboceanic weak asthenosphere [*Becker*, 2006] and nonlinear rheologies [*Jadamec and Billen*, 2010] have suggested alternative ways to explain the fast plate motion, not necessary requiring strong slabs.

[7] These works indicate that in order to comprehend the coupling between regional and global scales it is essential to improve the implementation

of the plate boundaries, and in particular to increase the resolution of the subduction zones to not more than 10 km, and possibly O(1) km. A first attempt to go in this direction has been done by *Stadler et al.* [2010] using adaptive multiscale finite elements. Here we show an alternative approach based on the Boundary Element Method, which combines high resolution with computational efficiency and is able to offer additional constraints on global plate motion modeling. This methodology aims at illustrating a new direction in which advancing 3-D spherical plate-mantle convection code.

[8] Our model parameters interest plate geometry and two viscosity ratios: plate versus upper mantle (η_{litho}) and lower versus upper mantle (λ). A vast number of works have pointed out that a reasonable range of values for η_{litho} is between two and three orders of magnitude, from models of subduction [*Funiciello et al.*, 2003a; *Bellahsen et al.*, 2005; *Schellart*, 2005; *Gerya et al.*, 2008; *Capitanio et al.*, 2009]. Estimates for λ instead vary between one and two orders of magnitude both from postglacial rebound [*Mitrovica*, 1996; *Lee et al.*, 2010] and from direct observation of plate velocities and mantle tomography. Direct constraints on lower mantle viscosity come from geoid studies [e.g., *Hager*, 1984], slab sinking rates [e.g., *Ricard et al.*, 1993], and more recently global reference frame reconstructions by *van der Meer et al.* [2010], who relates the position of slabs detected in mantle tomography with initiation and cessation of subduction constrained by kinematic models, allowing to derive an empirical average sinking speed of slabs in the mantle of 1.2 cm/yr. A similar statistical average on plate sinking in the upper mantle suggests instead a sinking rate of 5 to 10 cm/yr for a mature oceanic lithosphere [*Sdrolias and Müller*, 2006; *Goes et al.*, 2011]. While the ratio between these two values is not above 10, the hampering to the slab sinking speed in the upper mantle is due to the barrier formed by the upper-lower mantle discontinuity [*Capitanio et al.*, 2007; *Christensen and Yuen*, 1984; *Zhong and Gurnis*, 1995b], and considering that slabs in the lower mantle are likely less viscous and occupy a larger volume [*Zhong and Gurnis*, 1995a; *Morra et al.*, 2010], one obtains an indirect confirmation of a range for λ more likely above one order of magnitude, closer to the two orders of magnitude suggested by glacial rebound studies. We also observe that there is no reason for assuming that λ is independent from the speed of mantle flow. In fact, the rheological layering between upper and lower mantle likely depends on different creeping mechanism between the Olivine (and its polymorphs Wadsleyite and Ringwoodite) and Perovskite. If one or both these mechanisms are nonlinear, such as power law creep, λ will vary with the intensity of the dynamics and in particular be smaller for slower velocities (low strain rates). This motivates to test the largest variations in λ, from the minimum extreme $\lambda = 1$ up to $\lambda = 80$.

[9] We present two sets of models in spherical coordinates, modeling free surface (details in Appendix D), highly resolved slabs sharply separated from the mantle (Appendix B), linear distinct rheologies for lithosphere and mantle (Appendix C), and a smooth upper-lower mantle viscosity layering (Appendix A). In the first set of models we simulated plates characterized of a very large surface (square of Earth radius, R_{Earth}, and above), varying plate length (L_{litho}), plate width (W_{litho}), plate viscosity η_{litho} relative to the upper mantle viscosity (always normalized to $\eta_{\mathrm{UM}} = 1$), and upper lower mantle rheological layering ($\lambda = \eta_{\mathrm{LM}}/\eta_{\mathrm{UM}}$). Two types of behavior emerge, one for a weakly layered mantle ($\lambda \cong 1$) in which trench and plate motions are only slightly dependent from plate width (W_{litho}) while slab pull mainly controls plate motion if $L_{\mathrm{litho}} \leq R_{\mathrm{Earth}}$, while beyond this critical plate length ($L_{\mathrm{litho}} = R_{\mathrm{Earth}}$) the plate velocity largely decreases as well as its plateness, indicating an increase of stretching. Stronger mantle stratification ($\lambda \cong 10$ and above) induced a completely different behavior in which plate width (W_{litho}) becomes very important triggering simultaneous retreat and advance of different portions of the same trench due to constrained mantle flow and spontaneous folding of the slab due to shortening at depth in a spherical Earth. We synthesize this dynamics plotting plateness, which decreases with the emergence of lateral complexities in the plate deformation and the consequent stretching. With this value we aim to synthetize the wide range of deformations through which a plate can go, with the goal of understanding the conditions for plate fragmentation [*Bird*, 2003; *Sornette and Pisarenko*, 2003].

[10] Finally, we model plate motion based on reconstructed geometries of tectonic plates and their boundaries during the last 140 million years [*Gurnis et al.*, 2012], based on a rich set of marine geophysical data. We show that our Multipole–Boundary Element Method (MP-BEM) approach is able to capture the coupling between plate motions and induced mantle flow. Limiting our analysis to the $\lambda \cong 1$ case, our models show that the motion of Nazca, Pacific, Philippines, and Australian plates

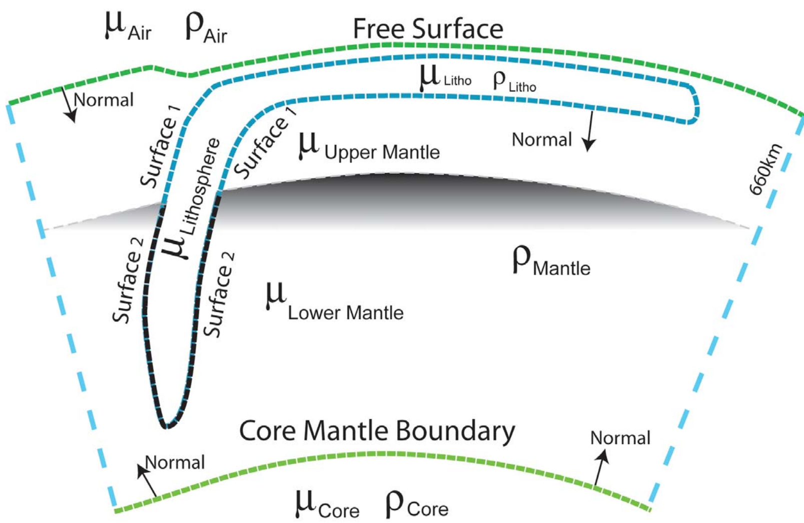

Figure 1. Setup. Sketch of the slab that subducts through a layered mantle. The main quantities indicated here are density (ρ) and viscosity (μ) for the main domains of interest, which appear in the boundary equations through their associated differential density ($\Delta\rho$) and viscosity ratio (λ). The free surface, core mantle boundary, and slab-mantle boundary are modeled with boundary integrals, while the viscosity transition at the upper-lower mantle boundary is assumed to be smooth (see left side of sketch) to allow using the approximation explained in Appendix A.

increases its agreement with the reconstructed velocities when all the plates are modeled simultaneously. Finally, surveying the cases definite by $\lambda \cong 1$ and $\lambda \cong 5$ and $\eta_{\text{litho}} = 100$ and $\eta_{\text{litho}} = 500$ (assumed $\eta_{\text{UM}} = 1$), we repeatedly find that the subduction of the Indian and Pacific plates, whose slabs where closer at an angle inferior to 90°, had a coupled dynamics. We suggest that the observed kinematic reorganization, which started because of unknown reasons in the Indian plate around 100 Ma [*Veevers*, 2000; *Wessel et al.*, 2006], propagated through this coupling to the Izanagi and than Pacific plate.

2. Numerical Method

[11] We model the planetary scale evolution of tectonic plates defined as isoviscous layer immersed in a mantle characterized by a radial viscosity profile (Figure 1). The density of the lithosphere in the model is constant and heavier than the mantle, inducing sinking in the mantle only after subduction is initiated, due to a thin lubrication layer between the lithosphere and the free surface of the Earth effectively producing a restoring force, which uplifts the slab and does not allow plates to sink in the mantle. Following *Morra et al.* [2007], the uplift is a natural and spontaneous outcome of the presence of a free surface as shown in the work by *Morra et al.* [2009], coherent with laboratory and other numerical models [*Funiciello et al.*, 2003a, 2003b]. A similar approach has been also adopted in 2D by *Ribe* [2010], in which, however, the slab is uplifted by the lubrication force exerted by a fixed (not free) upper bound for the mantle. The mantle is bounded by two free surfaces, one separating an external layer (representing either light sediments or water or air), and the second dividing the heavy core from the mantle (Figure 1). Differently from other Boundary Element works, a perturbative formulation has been introduced to reproduce the effects of a nonhomogeneous mantle (Appendix A for details). We use this approach for modeling the radial mantle structure, while the lateral heterogeneities are determined by the subducting lithosphere, explicitly defined by boundaries immersed in the mantle (Figure 1).

[12] We exclusively solve the equation of Stokes in distinct domains characterized by different viscosity and density, i.e., we neglect nonlinear rheologies (although the emerging result is often nonlinear due to the sharp domain boundaries, which are intrinsically nonlinear), and we do not explicitly consider the evolution of the thermal structure of the Earth. However, the model of the lithosphere that we adopt, as a "thin sheet," represents the upper thermal boundary layer of the convective mantle system. Our system therefore is able to adequately reproduce the tectonic forces that drive plate tectonics, embedding not only mantle induced forces by the sinking slabs as in other models of global mantle circulation [*Becker and O'Connell*, 2001; *Lithgow-Bertelloni and Richards*, 1998; *Conrad and*

Lithgow-Bertelloni, 2002], but also the essential propagation of the forces through the slab pull [*Zhong and Gurnis*, 1995a].

[13] In mathematical terms, for each bounded domain we use the definition of stress

$$\sigma = -pI + \eta(\nabla \mathbf{u} + \nabla^t \mathbf{u}) = -pI + \eta\dot{\epsilon}, \tag{1}$$

and we solve the generalized Stokes equations that comprise the momentum conservation and incompressibility condition:

$$\nabla \cdot \sigma + \rho \mathbf{b} = 0 \quad \nabla \cdot \mathbf{u} = 0. \tag{2}$$

[14] It has been proven that if the viscosity is constant in a domain D, these equations can be recast into a boundary integral formulation by *Ladyzhenskaya* [1963]. In simple terms, if D is the domain of interest, the velocity for each point in the interior of D can be expressed by the sum of two integrals called single and double layers, each summarizing the effect of the traction $\boldsymbol{\sigma}_{ik}(\mathbf{x})\mathbf{n}_k$ and velocity $\mathbf{u}_i(\mathbf{x})$ at the domain boundary ∂D, respectively [*Pozrikidis*, 1992, chap. 3; *Ladyzhenskaya*, 1963, pp. 55–60]:

$$-\frac{1}{8\pi\eta}\int_{\partial D}\sigma_{ik}(\mathbf{x})n_k G_{ij}(\mathbf{x},\mathbf{x}_o)dS(\mathbf{x}) + \frac{1}{8\pi}\int_{\partial D}u_i(\mathbf{x})n_k T_{ijk}(\mathbf{x},\mathbf{x}_o)dS(\mathbf{x}) = \begin{cases} u_i(\mathbf{x}_o) & \text{if } \mathbf{x}_o \in D \\ 0 & \text{otherwise} \end{cases} \tag{3}$$

where $\mathbf{G}_{ij}$ and $\mathbf{T}_{ijk}$ are the steady Green's functions for velocity and stress, respectively, also known as the Stokeslet and the Stresslet:

$$G_{ij}(\mathbf{x}-\mathbf{x}_o) = \frac{\delta_{ij}}{r} + \frac{\hat{x}_i\hat{x}_j}{r^3};\ \hat{\mathbf{x}} = \mathbf{x} - \mathbf{x}_o \text{ and } r = |\hat{\mathbf{x}}|$$

$$T_{ijk}(\mathbf{x}-\mathbf{x}_o) = -6\frac{\hat{x}_i\hat{x}_j\hat{x}_k}{r^5}.$$

[15] An extension of such formulation has been later proposed for a system composed by several domains in which the viscosity is different for each domain, but constant in each one. For example, following the classical formulation of *Pozrikidis* [1992, chap. 3] or the appendix of *Manga and Stone* [1995], the equation (3) can be written for the inner and the outer fluid, and combined in a unique boundary equation cast into a form more appropriate for a quasi-steady multiphase flows. Hence for a point $\mathbf{x}$ on the surface S that separates different fluids, we obtain the following:

$$\frac{1+\lambda}{2}\mathbf{u}(\mathbf{x}) - \frac{1-\lambda}{8\pi}\int_S^{PV}\mathbf{n}\cdot\mathsf{T}\cdot\mathbf{u}\,dS = -\frac{1}{8\pi\eta_0}\int_S \mathsf{G}\cdot\Delta\mathbf{f}\,dS, \tag{4}$$

where PV denotes the principal value of the integral, η_0 is the viscosity of the external fluid taken as a reference, $\lambda = \eta_{\text{int}}/\eta_0$ is the viscosity ratio between inner and outer fluid, and $\Delta\mathbf{f}$ is a normal stress jump that, assuming a radially oriented gravity field, simplifies to $\Delta\mathbf{f} = \Delta\rho(\mathbf{g}\cdot\mathbf{n})\mathbf{n}$, where g is gravity and $\Delta\rho$ is the differential density between inside and outside the boundary [*Morra et al.*, 2009]. This equation has been than extended for many surfaces with the same background, or nested one in each other. For a detailed technical treatise, see, for example, *Pozrikidis* [2002].

[16] Although there is no general agreement on how to modify the boundary equation (4) in order to model a nonhomogeneous domain, many methods have been proposed. We use a particular simple one, whose details are given in Appendix A, and we use it here only for modeling the upper-lower mantle viscosity transition, which we assume to be at a fixed depth and fixed viscosity jump. This assumption highly simplifies its approximated formulation and allows an exact esteem of the misfit between approximated and exact solution, once we assume a smoothly radially varying nonhomogeneous mantle viscosity.

2.1. Acceleration and Parallelization

[17] Equation (4) is a Fredholm integral equation of the second kind. In our numerical scheme, the plate surfaces are discretised into triangular elements. On each triangle the integral is calculated using analytical integration (see *Salvadori* [2010] for a review on all strategies for performing such integrals for any elliptic problem). The equation (4) is therefore said to be discretised in "Boundary Elements," also called "Panels," and the free model parameters (viscosity, density) are assumed constant on each panel in order to perform the analytical integration, and for this reason are sometimes called "Linear Boundary Elements." It has been shown that the linear system arising from the discretised integrals is well-conditioned and dense [*Zhu et al.*, 2006]; however, solving such system inverting its associated dense matrix is computationally inconvenient because the number of operations necessary to calculate the matrix itself scales as N^2, where N is the number of Panels. Many alternative approaches have been introduced in the last decade for building an equivalent matrix-vector multiplier operator [*Tornberg and Greengard*, 2008], including the fast multipole method [*Barnes and Hut.*, 1986] and the hierarchical matrix approach [*Börm et al.*, 2003; *Benedetti et al.*, 2008]. We use the

first approach, which offers potential advantages to tackle multiscale problems since it is compatible with 3-D unstructured surface meshes whose resolution can be adapted dynamically to track the physics of interest [*Morra et al.*, 2007]. The system is then solved employing an iterative GMRES algorithm [*Saad and Schultz*, 1986], which was tested and shown to converge also for large viscosity ratio, for the same setup tested in this work [*Morra et al.*, 2007]. The method has been finally parallelized using MPI libraries, and its efficiency on a Beowulf cluster has been tested up to 64 CPUs, still maintaining 90% of efficiency for each of the global integrals calculated in this work [*Morra et al.*, 2007]. We notice that the multipole approach allowed simplifying the communication between processors through the use of a shared (not distributed) tree to store all model information.

2.2. Time Stepping

[18] Time stepping is implemented with a Runge-Kutta second-order scheme. This means that the solution is calculated for the configuration at $t_{half} = t_n + \Delta t/2$, and then the "end of the step" updated configuration $X(t_{n+1})$ of the vertexes at the time $t_{n+1} = t_n + \Delta t$ is obtained displacing the nodes from $X(t_n)$ linearly the velocity solution at $t_{half} X(t_{n+1}) = X(t_n) + v(t_{half})*\Delta t)$. To satisfy convergence criteria of the solver, time step size is limited to keep the largest nodal displacement smaller than 0.1% of the Earth radius (0.001 R_{Earth}).

[19] The real time of the simulation can be calculated using the same scaling of *Morra et al.* [2010], i.e., the time factor is $\eta/(\Delta\rho \cdot g \cdot a)$ where g is gravity and a is a reference length. Our model runs with the renormalized values $\eta = 1$, $\Delta\rho = 30$, g = 1, a = 1 (Earth radius). Rescaled with the Earth typical values $\eta = 10^{21}$ Pas, $\Delta\rho = 80$ Kg/m^3, g = 10 m/s^2, a = 6 10^6 km, we obtain a scaling factor of 6 10^{12} s. Although each time step is different, the typical time steps are in the range 0.1–0.3, which correspond to about 0.02–0.06 Myr.

2.3. Plateness

[20] We employ the same definition of plateness of *Stadler et al.* [2010, chap. S8.1], who define it as the weighted average deviation of the plate velocity field from the best fitting rigid motion. Explicitly

$$P = 1 - \frac{1}{S}\int_S \frac{\|\mathbf{U}_r - \mathbf{U}_{bf}\|}{\|\mathbf{U}_r\|} ds,$$

where U_r is the computed velocity and U_{bf} is the velocity obtained from the best fitting Euler pole. S is the plate area. The norm $\|U_r - U_{bf}\|$ is defined as the root-mean-square (RMS) difference from the best fitting Euler pole.

[21] The plateness is calculated averaging 25 steps in order to avoid spurious oscillations due to the lagrangian mesh or effects related to the free surface. Because each time step has a different length (see the previous paragraph) the time interval on which plateness is averaged varies during each simulation and with each model, however, around 1 Myr (0.5–1.5 Myr) for an upper mantle viscosity of $\eta = 10^{21}$.

2.4. Construction of the Plates

[22] In order to build the initial conditions for the simulations at present time and 100 Ma, we use the open source plate tectonic software GPlates version 1.0 and the GPlates Markup Language (GPML) to represent global plate reconstructions [*Gurnis et al.*, 2012]. Initial conditions for the models are built from reconstructed plate geometry in 3D, with age-defined thickness for different material parameters including plate density and viscosity (L. Quevedo et al., manuscript in preparation, 2012). The present-day model consists of surface models of 13 major plates: Africa, Antarctica, Arabia, Australia, Caribbean, Cocos, Eurasia, Nazca, North America, Pacific, Philippines, Scotia, and South America. The slabs are extrapolated into the mantle taking into account the last 20 Myr of subduction history. Oceanic crust and continental crustal thickness was sampled separately. The continental was taken from the TC1 model [*Artemieva*, 2006]. A gap of 50 Km around each plate was further imposed to the model preventing immediate contact between the surfaces.

[23] The 100 Ma model was derived from 20 Myr of tectonic evolution (from 145 Ma to 125 Ma) of the 10 major plates at the time: Africa, Eurasia, India, North America, Phoenix, East Gondwana, Farallon, Izanagi, Pacific, and South America. Oceanic crust thickness was obtained by sampling the age grid associated with the reconstruction at resolution, while continental crustal thickness was at 120 Km. A gap of 200 Km around each plate was imposed to the model.

3. Model Results and Analysis

[24] We rescale the Earth radius to 1, resulting in a mantle thickness to 0.5 and an upper lower mantle transition located at $R_{\mathrm{ULM}} = 0.85$. The surfaces

Table 1. Definition of the Symbols and Their Units

Symbol	Units	Meaning
		Physical Quantities
$\boldsymbol{\sigma}_{ij}$	N/m^2	Stress tensor
$\boldsymbol{t}_i$	N/m	Traction
$\boldsymbol{n}_i$	-	Normal (to the element)
$\boldsymbol{u}_i$	m/s	Velocity
$\boldsymbol{G}_{ij}$	(m/s)/N	Stokeslet (Green function of the velocity)
$\boldsymbol{T}_{ijk}$	(N/m^2)/(m/s)	Stresslet (Green function of the stress)
		Parameters
γ	-	Ratio between viscosities external to the same surface (for example, between lower and upper mantle)
λ	-	Ratio between inner and outer viscosities to a surface (for example, lithosphere viscosity, or core viscosity)
η_{litho}	Pa s	Background viscosity (of the lithosphere)
η_{UM}	Pa s	Background viscosity (of the upper mantle)
η_{LM}	Pa s	Background viscosity (of the lower mantle)
$\mathbf{W}_{\mathrm{litho}}$	m	Lithospheric width for a rectangular plate (length of the trench)
$\mathrm{L}_{\mathrm{litho}}$	m	Lithospheric length for a rectangular plate (perpendicular to the trench)
D_{eq}	Pa s	Equilibrium distance between surfaces (i.e., the contact algorithm will displace the node of the "slave" at this distance from the "master" surface).
		In all models equal to $\mathrm{L}_{\mathrm{litho}}$.
$\mathrm{D}_{\mathrm{int}}$	Pa s	Interaction distance between two surfaces (i.e., above this distance the contact algorithm does not apply).
		In all models equal to 2*$\mathrm{L}_{\mathrm{litho}}$.
μ	Pa s	Outer viscosity $\eta_{\mathrm{OU}} = 0.01 * \eta_{\mathrm{UM}}$
μ_1	Pa s	Outer viscosity (above the 660 boundary)
μ_2	Pa s	Outer viscosity (below the 660 boundary)

delimiting the mantle-air external boundary and the mantle-core boundary are free to evolve following the solution of the momentum equation. The scaled viscosity and lithosphere-mantle differential density are $\eta = 1$ and $\Delta\rho = 30$, respectively (Table 1 for other model parameters). With this choice, the Earth-air free surface displays a dynamic topography of about one order of magnitude higher of the real Earth.

[25] We investigate two model setups. The first consists of the subduction of rectangular plates, for which we vary plate width ($\mathrm{W}_{\mathrm{litho}}$), length ($\mathrm{L}_{\mathrm{litho}}$), and viscosity ($\eta_{\mathrm{litho}}$), into a uniform or layered mantle for which we vary the upper-lower mantle viscosity ratio ($\lambda = \eta_{\mathrm{LM}}/\eta_{\mathrm{UM}}$). We first show the effect of the plate size ($\mathrm{W}_{\mathrm{litho}}$ and $\mathrm{L}_{\mathrm{litho}}$) to plate velocity and plateness and than study the combined effect of plate viscosity (η_{litho}) and upper-lower mantle layering (λ). The second setup is based on plate reconstructions. Initial conditions at the global scale are based on reconstructed plate geometries of 25 Ma and 125 Ma (see Figure 2 and Quevedo et al. (manuscript in preparation, 2012) for more details on the reconstruction). The models are run long enough to stabilize the plate motion allowing the comparison of the modeled plate velocities with the reconstructed ones. In order to estimate the role of slab-slab interaction for global plate tectonics, we compare the results of the observed kinematics resulting from the dynamics of each separate plate with the one obtained from the simulation involving all plates simultaneously. Finally, we show that the coupling between the Izanagi and India plate is sufficiently intense to suggest that played a role in the global plate reorganization of about 100 Ma.

[26] The complexity of the models employed here requires a choice on a number of numerical parameters that are discussed in detail in Appendix A (implementation of upper lower mantle transition), Appendix B (resolution tests), Appendix C (plate viscosity), and Appendix D (free surface algorithm). All the parameters employed are summarized in Table 1 and were consistently used in all the models, except where we explicitly varied a particular one in order to study its role. As shown in Appendix D, choosing the parameters associated with the free surface can enhance or hamper trench retreat, in agreement with some recent results from modeling subduction with a free surface [*Morra et al.*, 2007; *Schmeling et al.*, 2008; *van Dinther et al.*, 2010; *Ribe*, 2010]. Our choice was to hamper, however without inhibiting it, trench motion because we are interested in the dynamics of very large plates for which the average observed trench motion in the past 100 Myr [*Sdrolias and Müller*, 2006] is no more than 10% of the overall plate motion [*Goes et al.*, 2011]. We remark here that in our models the trench can migrate, and in fact we show that the introduction of a strong upper-lower mantle layering triggers trench migration, in agreement with past numerical models [*Stegman et al.*, 2006; *Schellart et al.*, 2007; *Di Giuseppe et al.*, 2008; *Stegman et al.*, 2010a].

 10.1029/2011GC003843

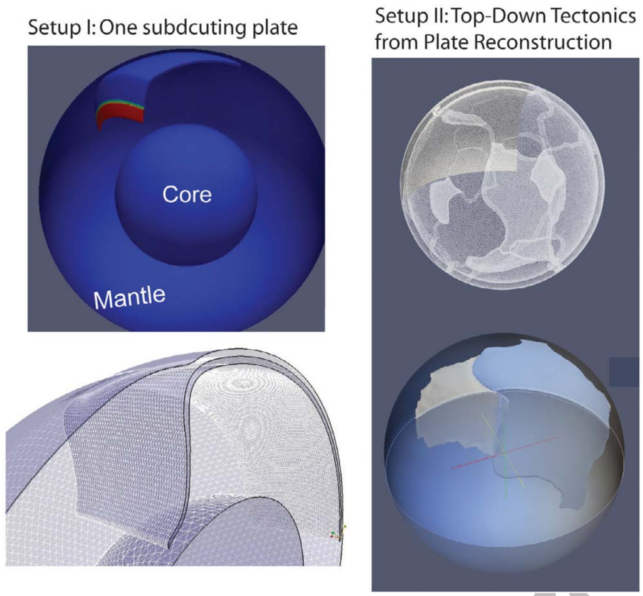

Figure 2. (left) The numerical setup for the subduction of a single plate. The top left figure indicates the initial conditions. The red portion of the slab is the one that is already in the lower mantle. For this reason, many models with a strong upper-lower mantle transition display the "pinning" of the slab in the lower mantle. The bottom left figure shows a mature subduction in a homogeneous mantle. (right) Shown at top is the 3-D expression of the plate boundaries through the CGAL meshing utilities, modified following the method introduced by Quevedo et al. (manuscript in preparation, 2012), postprocessed with GPlates. The database employed for the plate boundaries is the one of *Gurnis et al.* [2012]. The bottom right figure is a detailed plot of the Nazca–South America plate interaction, where the colors indicate convergence velocity (plate speed in the direction of convergence). The 3-D setup is cut in order to show the morphology of the slab. More details on the contact algorithm responsible for the inter-plate interaction are given in Appendix D.

3.1. Subduction of a Rectangular Plate in a Homogeneous Mantle

[27] We model the subduction of plates with constant viscosity and constant thickness in a homogeneous mantle. The parameters chosen are displayed in Table 2. Sizes vary from 0.5 to 2 times the Earth radius, both in width and length (W_{litho} and L_{litho}). Models do not reach steady state (but they all start with the same initial slab length, see Figure 1), and the velocities and plateness are calculated at the same time after few hundred time steps, when any initial transient effect becomes negligible. Transient effects arise from the fact that each model starts with no surface topography, but with a perfectly spherical Earth. The isostatic equilibrium is reached after the first few tens of steps. When the topography of equilibrium is reached the associated velocities diminishes, the length of each time step increases, and the geodynamic configurations and dynamics topography evolve together.

[28] We find that for this homogeneous mantle setting, L_{litho} strongly controls plate kinematics while W_{litho} has a small effect (contrary to a strongly layered mantle as we will show later in the paper). A top view of the dynamic evolution of the free surface velocity (white segments) and of the plateness (see numerical methods) is shown in Figure 3. We find strong decrease of plate speed with the increase of L_{litho}, with plate velocities decreasing of a factor three while plate length increases from 0.5 to 2 times R_{Earth}. On the contrary, plate speed is only weakly dependent on W_{litho}, with a slight favor for wider plates that travel faster then smaller ones. Streamlines associated to the mantle flow of two models, one with a short

Table 2. Variable Parameters Tested in the Rectangular Plate Models

Quantity	Values Tested (Only Some Combinations Tested)
W_{litho}	0.5, 1.0, 1.5, 2.0 (× Earth radius)
L_{litho}	0.5, 1.0, 1.5, 2.0 (× Earth radius)
η_{litho}	100, 200, 500 (× mantle viscosity)
$\lambda = \eta_{LM}/\eta_{UM}$	1, 2, 3, 5, 10, 20, 40, 80

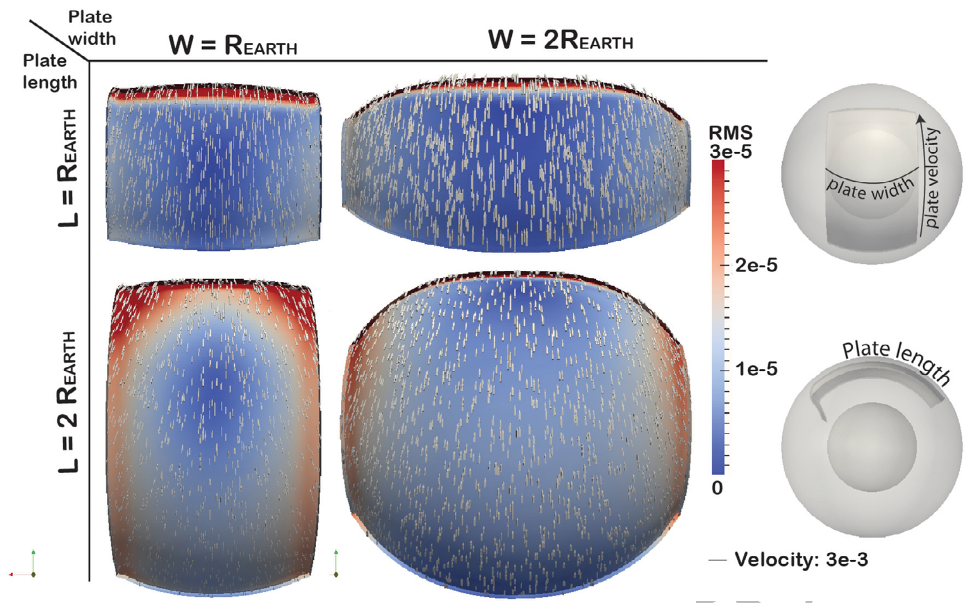

Figure 3. Top view of the plateness for four rectangular models, where the color scale measures the RMS of the local horizontal projection of the velocity versus the rigid average plate velocity, calculated through a best fitting Euler pole. Red (high RMS) implies a strong departure from the average speed, while blue is coherence with the average. The velocity is instead displayed as arrows, whose length is proportional to the corresponding (nondimensional) plate speed, whose reference is shown in the bottom right of the figure. The clearest observation is that for wide plates the main source of reduced plateness is the distance from the plate axis (intended as the direction of subduction). This is partly due to the converging velocity (a "sinking" effect) and partly due to the slowness of the plate far sides due to the minor distance from the local Euler axis of rotation. The most striking observation is the emergence of a length scale along the axis of subduction. Plates with a length inferior to two times the mantle thickness display an excellent plateness (i.e., a low RMS), while longer plates are characterized by a drop in RMS, indicating the propensity of the plate for fragmentation.

plate (L_{litho} = 1; W_{litho} = 1) and one with a long plate (L_{litho} = 2; W_{litho} = 1), are shown in Figure 4. The pattern designed by the first model indicates the generation of a strongly poloidal convective cell accommodating the plate motion, hence minimizing the drag at the base of the plate. The flow induced by the long plate, instead, displays a complex 3-D pattern, coherent only with the frontal portion of the plate, while the drag at the base of back of the plate is opposing plate motion, triggering the observation of a plate stretching, synthesized in low plate velocity and high plateness (Figure 5).

[29] *Funiciello et al.* [2003b] and *Capitanio et al.* [2007] have shown that the sinking velocity is mostly independent of plate strength and trench motion. This was confirmed for very large plates by *Stegman et al.* [2006], although with complexities in trench migration. We find here that this relationship breaks down for very long plates, and this critical length is $L_{litho} > R_{Earth}$ for Earth-like spherical coordinates and assuming no mantle layering.

[30] In Figure 3, the RMS deviation between the local velocity and best fitting plate velocity is displayed for 4 representatives (L_{litho} = 1 and 2, W_{litho} = 1 and 2) of a total of 16 rectangular modeled cases (L_{litho} = 0.5, 1, 1.5, 2 and W_{litho} = 0.5, 1, 1.5, 2) summarizing the causes of the breakdown of plate speed for very long plates. For the longer plates, the velocity decreases from the trench toward the trailing edge. This is indicated by the RMS deviation: the fast velocity at the trench areas are red because the velocities are faster of the average, blue in the middle because the same as average and again red at the edge because much less than the average, implying a strong stretching. These results suggest that in a homogeneous mantle for small values of L_{litho} the plateness is higher and the velocity uniform, while for large values of L_{litho} (above that critical length R_{Earth}) the plate-mantle coupling changes and the plate velocity drastically diminishes. We find that the transition for a homogeneous all mantle is around the threshold value $L_{litho} = R_{Earth}$, implying that a smaller value, roughly corresponding to twice the thickness of the uppermost layer (for

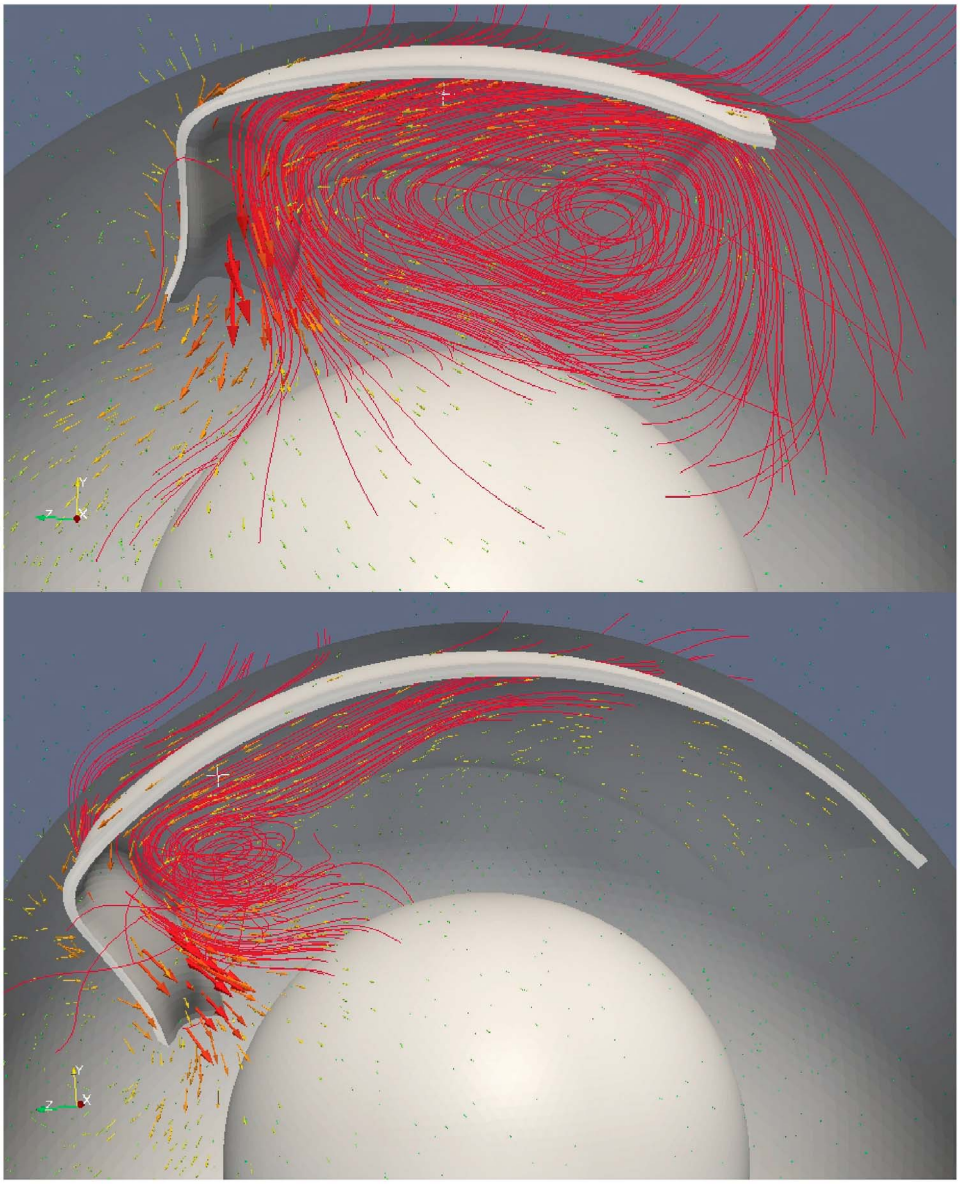

Figure 4. Three-dimensional mantle flow reconstructed for two rectangular plates, both with a width equal to Earth radius (W = 1). (top) The flow for a plate length that is 1 times the Earth radius (L = 1); (bottom) the oblique view of the flow with a plate whose length is 2 times the Earth radius (L = 2). The shorter plate displays a distinct induced cell in the mantle flow. The strong mantle flow induces the eye of the vortex close to the end of the plate. Figure 4 (bottom) shows a more complex scenario in which the flow only partially raises back forming a cell, and partially flows laterally to the plate, in proximity to the core. This implies that a long plate will undergo a stronger basal friction, in case of full plate-mantle coupling (i.e., no low-viscosity zone at the base of the plate).

example, $L_{litho} = 2T_{UpperMantle} \sim 1300$ km for a strongly upper-lower mantle viscosity transition) is expected for a strongly layered mantle.

[31] From this observation we conclude that a very wide plate will tend to break or fragment for lengths beyond R_{Earth}, when the entire mantle is involved in its motion, if the stresses involved are sufficiently high. Such stresses can be calculated straightforwardly from the model outcomes. For a lithosphere of viscosity about two orders of magnitude more viscous than the mantle, the plate velocity completely decays from the trench to a distance of R_{Earth}, therefore taking the sinking velocity of the order of the one of the Pacific plate $V_{Pacific} = 10$ cm/yr), one obtains an average lithospheric strain rate equal to $\varepsilon = V_{Pacific}/R_{Earth} = (3 \cdot 10^{-9}/6 \cdot 10^{6})\ s^{-1} = 5 \cdot 10^{-16}$. Assuming a

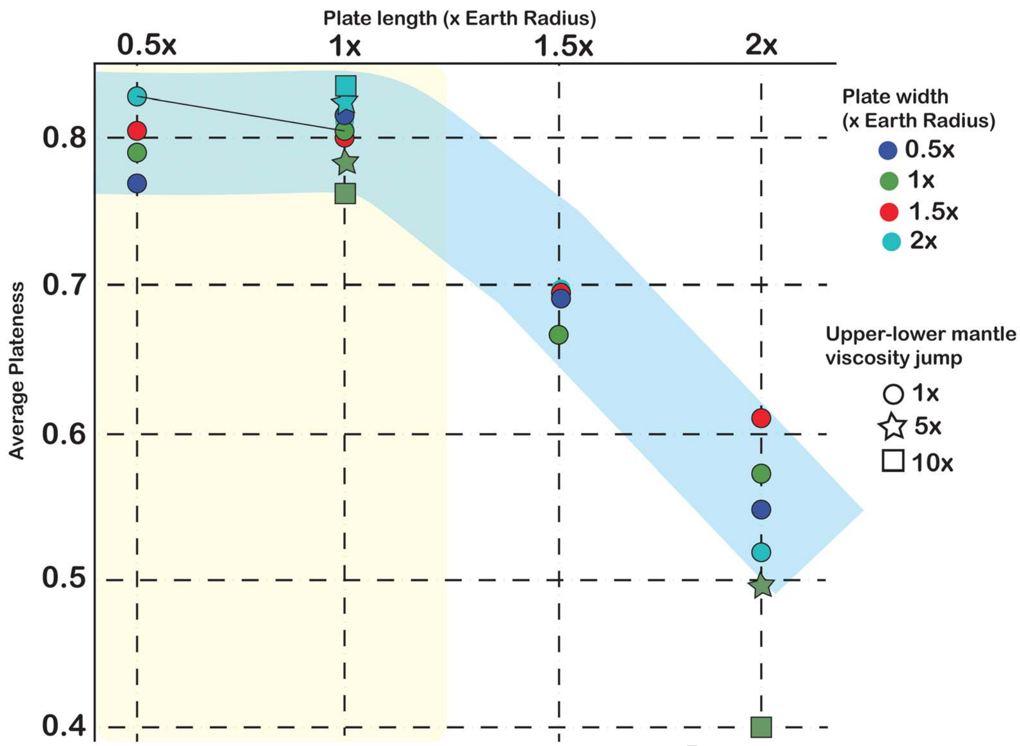

Figure 5. Average plateness versus plate length. Summary of the plateness (see method to see how it is calculated) for the models with homogeneous mantle and few models with a nonhomogeneous mantle to show the similar pattern. The main feature is the flat behavior for slab length inferior to Earth radius when the plateness is maximum and relatively independent from plate length. Above the Earth radius threshold, the plateness drops drastically and steadily. This phenomenon remains also for different plate viscosities and thicknesses, while it is strongly perturbed by a high upper-lower mantle viscosity jump, as better shown in Figure 6.

lithospheric rheology 100 times higher of the mantle, and a mantle one of 10^{21} Pas, the emerging lithospheric stresses are of the order of $2\eta_{\text{litho}}\varepsilon = 2 \cdot 10^{23} \cdot 5 \cdot 10^{-16}$ Pa = 100 MPa, which are slightly less of the typical rupture stresses found in global plate tectonic models for estimating the "rupture stress" in tectonic systems [*Regenauer-Lieb et al.*, 2001; *Tackley*, 2000b; *Trompert and Hansen*, 1998].

[32] A second increase of RMS deviation (and therefore drop in plateness) occurs laterally from the plate axis. We find that this is due to three superimposed effects: (1) for very wide plates the speed of the plate at its lateral edges is much lower due to the constant angular velocity but minor distance from the Euler axis (v = w × r); (2) wider plates display a larger change in the flow direction at the plate sides toward the center of the trench, generating a "sinking" effect that diminishes plateness; (3) the wider the plate is, the less is its coherence, because the stresses decay with the distance.

3.2. Role of Plate Viscosity and of Mantle Layering

[33] We repeated a selected set of the above subduction models, testing plate viscosity values (η_{litho}) of 100, 200 and 500 times the upper mantle, and lower-upper mantle viscosity ratio λ between 1 and 80 (see Table 3 for a detailed list of the performed models). The resulting plateness versus L_{litho} and plateness versus λ are shown in Figures 5 and 6, respectively. Comparing the two plots shows that the strong dependency of plateness from L_{litho} and the weak one from W_{litho} is here confirmed, but it tends to break down for high λ. In fact, from Figure 6 clearly emerges that the plateness decays increasing λ when λ is about above 10. This result is further analyzed in section 5.

[34] A careful investigation of the causes of such behavior for each model indicates that for $\lambda = 5$ and less the plate sinks in a similar way as for a homogeneous mantle, while for values of $\lambda = 10$ and above the trench exhibits a laterally heterogeneous behavior, partially advancing and partially

Table 3. List of the Values Chosen for Each Rectangular Plate Model

Model	L_{litho}	W_{litho}	η_{litho}	$\lambda = \eta_{LM}/\eta_{UM}$
1	1.0	1.0	100.0	1.0
2	1.0	1.0	100.0	2.0
3	1.0	1.0	100.0	3.0
4	1.0	1.0	100.0	5.0
5	1.0	1.0	100.0	10.0
6	1.0	1.0	100.0	20.0
7	1.0	1.0	200.0	1.0
8	1.0	1.0	200.0	2.0
9	1.0	1.0	200.0	3.0
10	1.0	1.0	200.0	5.0
11	1.0	1.0	200.0	10.0
12	1.0	1.0	200.0	20.0
13	1.0	1.0	200.0	40.0
14	1.0	1.0	200.0	80.0
15	1.0	1.0	500.0	1.0
16	1.0	1.0	500.0	2.0
17	1.0	1.0	500.0	3.0
18	1.0	1.0	500.0	5.0
19	1.0	1.0	500.0	10.0
20	1.0	1.0	500.0	20.0
21	1.0	2.0	100.0	5.0
22	1.0	2.0	100.0	10.0
23	1.0	2.0	100.0	20.0
24	1.0	2.0	200.0	5.0
25	1.0	2.0	200.0	10.0
26	1.0	2.0	200.0	20.0
27	1.0	2.0	200.0	40.0
28	1.0	2.0	200.0	80.0
29	1.0	2.0	500.0	5.0
30	1.0	2.0	500.0	10.0
31	2.0	1.0	200.0	1.0
32	2.0	1.0	200.0	3.0
33	2.0	1.0	200.0	5.0
34	2.0	1.0	200.0	10.0

retreating, depending on the plate width and strength. This result is an agreement with the complex trench morphology found in the work of *Stegman et al.* [2006] for plates up to 8000 km, but it shows here that for wider plates the advancing versus retreating pattern is not from the edges versus the slab center, but it has a specific lengthscale, of the order of the Earth radius. Two examples of the trench morphology after a long subduction time are illustrated in Figure 7, exactly for the cases (W_{litho} = 1; L_{litho} = 2) and (W_{litho} = 2; L_{litho} = 1). We therefore find that one order of magnitude of lower-upper mantle viscosity ratio λ is the critical value for observing a strong tectonic effect of mantle layering.

[35] Finally, we also observe a milder, but clear influence of the plate viscosity η_{litho} on plateness. In particular, we notice a general tendency of the strong plates to display higher values of plateness, and we also find that stronger plates display a larger spectrum of plateness values. A detailed analysis of the models displaying such pattern has shown that a very low plateness was observed in correspondence to strong trench migration, in particular the higher the viscosity, the more common is observing advancing trenches. This observation is coherent with laboratory experiments [*Bellahsen et al.*, 2005].

3.3. Subduction Simulations of Reconstructed Plates

[36] In most papers treating the dynamics of subduction the downgoing plate has a very simple geometry, usually derived from a rectangular shape. In our setup the small-scale variations of the plate morphology play a negligible role in the dynamics of subduction. The model starting from reconstructed geometries in fact shows how only the first order complexities due to the plate shape influence the outcoming plate kinematics.

[37] We started the models with two distinct reconstructed geometries (Quevedo et al., manuscript in preparation, 2012), 25 Myr before present and before 100 Ma, respectively, running the models for at least 250 time steps, equivalent to 10–20 Myr (depending on the assumed upper mantle viscosity, see time stepping in methods for more details), allowing our models to reach the conditions in proximity to the 100 Ma reorganization and to present time. We found that this was always sufficient to reach a stable solution, determined by the reorganization of the morphology of the subducted slabs. However, we stress here that this is not a steady state solution, as the system is not expected to reach such state. In the present configuration the main four subducting plates are Pacific, Nazca, Australia and Philippines while at 10 Ma they were Izanagi, Farallon, Phoenix, and India. The plate configurations in these two periods are exceptionally different. The size of the four main plates at 100 Ma is very close, while at present time are strongly differentiated. The causes of this difference are covered in a companion paper (G. Morra et al., Hierarchical self-organization of tectonic plates, submitted to *Nature Geoscience*, 2012). The morphology of Izanagi, Farallon and Phoenix plates at 100 Ma is comparable to the model in Figure 3 (top right), as they subduct on the long side and have a similar shape; India, on the contrary, is a long narrow plate subducting along its short side, like the one in Figure 3

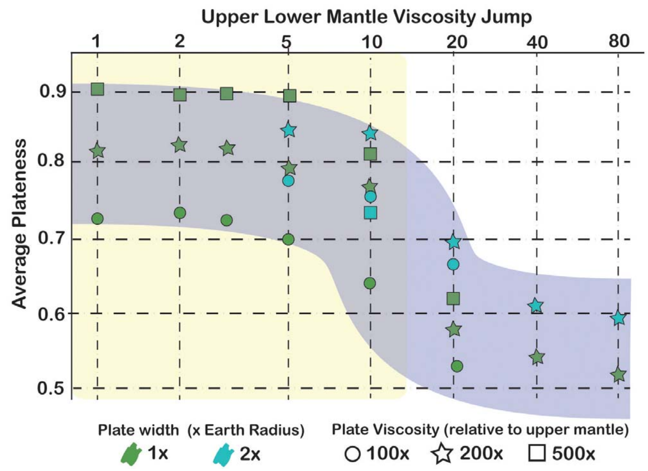

Figure 6. Average plateness versus upper-lower mantle viscosity jump. Two patterns emerge. The first is the systematic increase of plateness with the raise of plate viscosity, which is a predictable consequence of the strength of the plate. The second is a critical behavior of the plateness versus viscosity jump. This is indicated by the bluish area and shows that until about a viscosity ratio of 10 the plateness, and therefore the surface expression of plate tectonics, shows a small sensibility from the λ, while for greater values of λ, the plateness dramatically drops to a new plateau that indicates a strongly deformed plate. In fact, as displayed in Figure 7 for such values of λ, the morphology of the trench becomes highly heterogeneous and assumes advancing and retreating modes. On the contrary, when the upper-lower mantle viscosity jump is less than 10, the plate simply subducts in the lower mantle, although at lower speed.

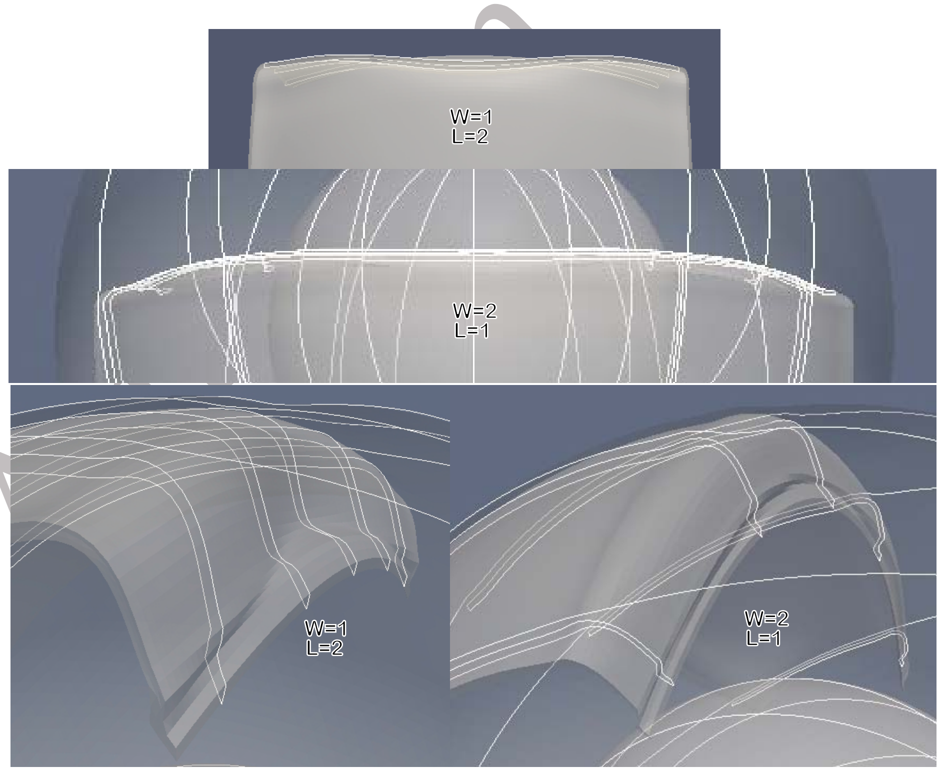

Figure 7. Plots depicting the trench and slab morphology of plates subducting in a strongly layered mantle. (top and middle) These plots represent subduction of a plate with width equal to one time (W = 1) and twice Earth radius (W = 2), respectively. The morphology as displayed by the sections shows an oscillation between advancing and retreating trenches, with a length scale of the order of 1 (R_{Earth}). (bottom) These plots clarify the mechanism behind this dynamics: the initial pinning of the slab in the lower mantle, combined with the lack of space at depth due to the Earth sphericity induces plate folding, as already suggested in the work of *Morra et al.* [2009].

10.1029/2011GC003843

(bottom left). The morphology of the plates at present is very heterogeneous: the Pacific plate is much bigger than all the other plates in the present and past times; Australia, Nazca and Philippines are of gradually decreasing size; Australia has the shape of a wide rectangle, and Nazca and Philippines are relatively square. The results of the rectangular plates already illustrate how the geometrical differences play a major role in controlling regional geodynamics of the very big plates, we expect these differences to appear in the global models.

4. Modeled Plate Velocities Versus Plate Kinematics

[38] With the exception of the Pacific plates, a very high plateness characterizes all the modeled subducting plates, with a low RMS deviation from the best fitting rigid velocity. This is coherent with the expectations of the rectangular plate models. We therefore focus on the match between the reconstructed and modeled velocities, and whether the purely dynamic numerical models (i.e., without any kinematic imposition) are able to match the plate velocities. In particular we do not attempt to match plate velocities changing plate rheology or mantle rheology, as the number of parameters available would certainly allow us to match the available observables with a large set of parameters values, but without gaining any particular physical insight; instead we compare the direction of motion of the simplest model characterized by a uniform highly viscous lithosphere above a homogeneous mantle down to the core with the observed (present) or reconstructed (100 Ma) direction of motion. Such a match is obtained by calculating the best fitting Euler pole of the deforming modeled plates (not being rigid) and normalizing (scaling) the average plate speed. In this way we characterize which plate motions are compatible with the modeled slab pull and which are not.

[39] We do not attempt to model plate boundary migration, for two reasons: the trench motion in our numerical models is strongly dependent on free model parameters and the reconstructed plate boundaries are uncertain due to the assumption of undeformabale shape, introducing a substantial error in the location of the boundary far in the past. Furthermore, the main outcome of the model is plate velocity direction. Furthermore, our understanding (and the quality of the model) of trench migration is very poor, therefore, our ability to exactly model trench position is very low. However, because trench migration is, averaged in the long-term, a minor component of plate motion [*Goes et al.*, 2011; *Sdrolias and Müller*, 2006; *Torsvik et al.*, 2008], we are allowed to analyze only plate kinematics, as commonly done in global geodynamic models emerging from the pull of the subducted slab [*Conrad and Lithgow-Bertelloni*, 2002]. As the slab pull is controlling plate motion, and it is determined by the plate's history, such comparisons can be seen as tests the quality of the plate reconstruction itself.

[40] Figure 8 illustrates models of plate velocities at the present time with a homogeneous mantle (λ = 1) focusing on the largest four subducting plates: Australia, Nazca, Philippines, and Pacific. Three models for a fully coupled mantle simulation are shown. A rough modeled plate velocity of all the plates together (Figure 8, top), where the outcome of the collective plate motion shows a strong hampering of the plate velocity due to basal drag, and the Pacific plate is much slower than observed, suggesting the necessity of a strong low viscosity zone, as suggested by past mantle convection [*Tackley*, 2000a] and global geodynamic models [*Becker*, 2006]. We compare this model with the separate simulation of subduction of the four main plates: Australia, Nazca, Philippines, and Pacific. The intensity of the velocities shown in Figure 8 (middle) is renormalized (not affecting the direction), in order to focus on the observed magnitude of plate velocity, as opposed to the direction. Physically this is equivalent to adapting an ad hoc (different plate by plate) low-viscosity zone at the base of each plate, or to remodulate slab pull in function of whether the slabs are coherent, or to inhibit the pull of the slabs in the lower mantle. This allows us to observe that the kinematically modeled direction of plate motion is fairly similar to the observed one, with some stronger discrepancies for the Pacific plate. Finally in the last plot (Figure 8, bottom) we show the renormalized arrows of the same flow of Figure 8 (top), allowing us to directly compare the results with the model (Figure 8, middle). In addition to the reasonably good agreement with kinematically modeled plate motion, we observe that the interaction between the motion of the Pacific and Indian plates changes their plate motion direction remarkably, indicating an intense interaction between plates through a collectively driven mantle flow. The full study of the entire parameter space related to the reconstructed models will require modulating plate buoyancy, plate viscosity and upper-lower plate

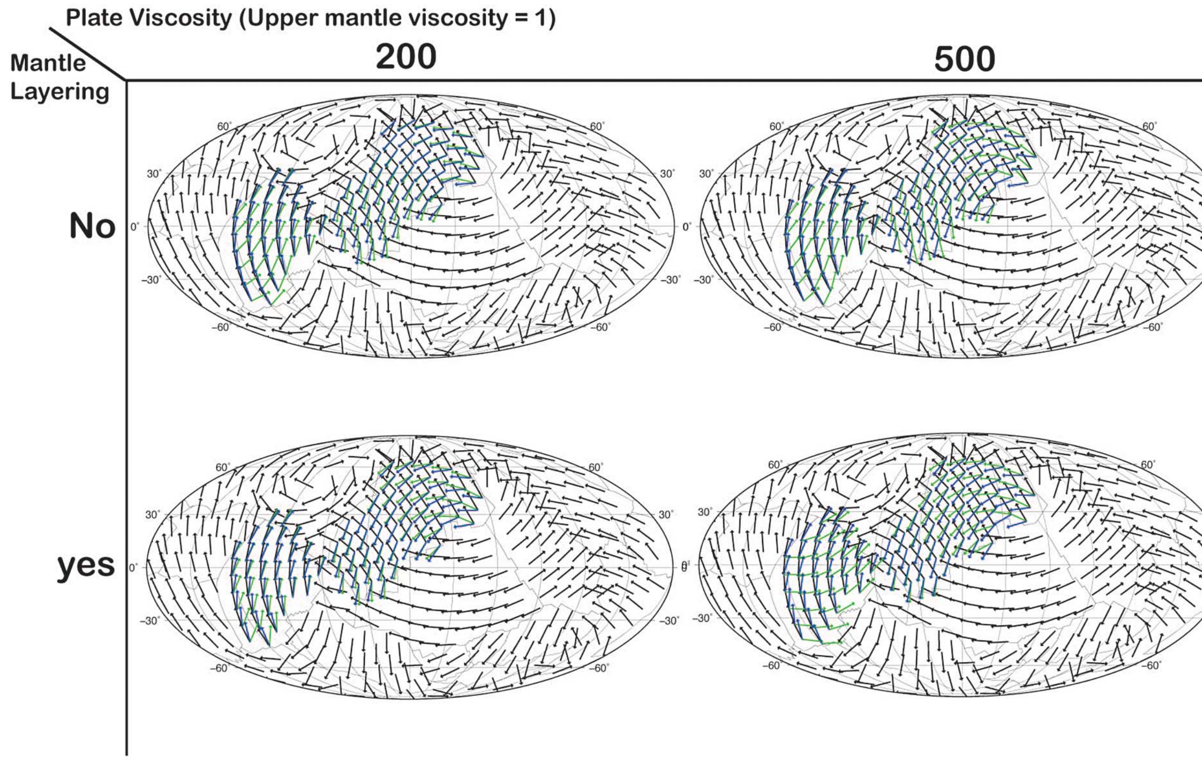

Figure 8. Comparison of the modeled velocity vectors (red) for present plate geometries. Three models are shown. (top) The rough plate velocity outcome for the model of the collective plate motion (i.e., one simulation embedding all the plates), where we observe that the biggest plates, move slower as the basal drag is greater. (middle) The outcome of the separate plate motion for each of Australia, Nazca, Philippines, and Pacific plates (i.e., the subduction of each of these plates is modeled without the presence of the other plates). Here the velocity is renormalized in order to match the observed intensity of plate velocity, so the only information arising from the models is the direction. (bottom) The collective plate motion of the top, but with rescaled velocities. Besides the more or less good agreement with plate motion, we observe the interaction between the motion of the Pacific and Indian plates, whose direction converge when modeled collectively.

viscosity ratio, and is the topic of a forthcoming work, now in preparation.

[41] Focusing on the 100 Ma plate reorganization, Figures 9 and 10 display the results of the comparison of reconstructed versus modeled plate velocities and slab morphology for the India and Izanagi plates around 100 Ma. In Figure 9, the blue arrows represent the single plate velocity (i.e., the velocity of each plate modeled separately) while the green arrows the coupled system (i.e., the velocity of each plate when one model with the two plates simultaneously are performed). Differently from the present-day models, we investigate here both the role of plate rheology and mantle layering. We observe a systematic agreement between the reconstructed and modeled plate velocities for India, while there is a systematic discrepancy between modeled and reconstructed velocities for the Izanagi plate. This discrepancy does not necessary imply that the model is wrong, as the reconstructed kinematics from 125 to 80 Ma undergoes a strong 180 degrees rotation, and the reconstructions of absolute plate motions at that time are constrained by sparse data only. We observe furthermore that the global plate reconstruction goes through a switch of reference frame at exactly 100 Ma, which add uncertainties to the reconstruction [*Wessel and Kroenke*, 2008; *Mjelde and Faleide*, 2009]. It is in fact unknown to what extent the fixed hot spot hypothesis holds for this time period, and so far no reliable geodynamic models have been developed to test Pacific hot spot fixity for times before 80 Ma.

[42] The most important outcome of this model is the robust detection of an interaction between India and Izanagi plates. We always observe a change of

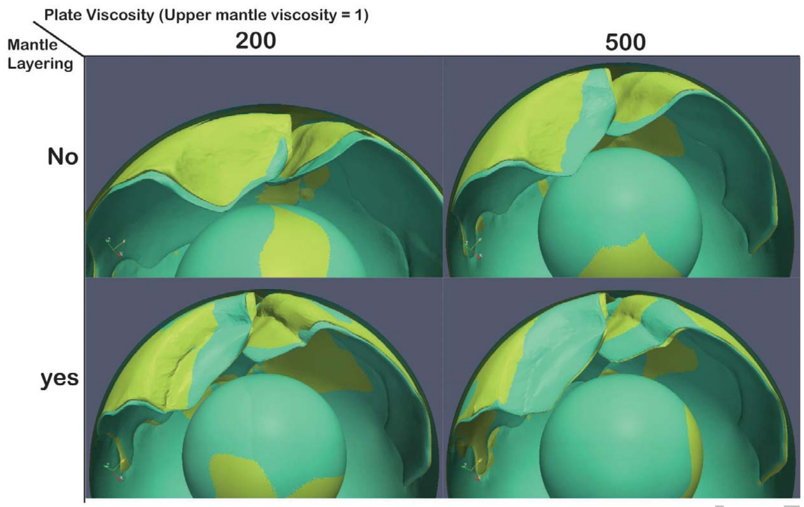

Figure 9. Comparison of reconstructed versus modeled plate velocities for India and Izanagi around 100 Ma. Blue arrows represent the single plate velocity while the green arrows the coupled system. Reconstructed velocities for India are reproduced properly, while there is a systematic discrepancy between modeled and reconstructed 100 Ma velocities. This discrepancy does not necessary implies that the model is wrong, as the reconstructed kinematics from 125 to 80 Ma undergo a strong 180 degrees rotation that probably requires better constrains. Furthermore, the reconstruction undergoes a switch of reference frame at exactly 100 Ma, which add uncertainties to the validity of the reconstruction velocities. In this sense, the modeled velocities are probably more reliable. The most important result is the deviation between coupled and uncoupled plate motion. In fact, this difference proves that the plates interact with each other. This interaction is a strong candidate to explain the globalization of the 100 Ma plate reorganization that started in the Indian basin.

plate motion from single to coupled configurations for any condition, with an homogeneous ($\lambda = 1$) or layered mantle ($\lambda = 5$), and a plate viscosity varying from $\eta_{\text{litho}} = 200$ to $\eta_{\text{litho}} = 500$. We do not know which triggering event initiated the change of direction of motion of the Indian plate, however our results indicate that Indian and Izanagi slabs interacted and that such interaction had to reflect into surface plate motion. Therefore when one of the two plates changed its kinematic, this must have reflected to the change in the other plate, producing the propagation of the 100 Ma plate reorganization of India to the Pacific Basin [*Veevers*, 2000].

[43] In Figure 10 we show more in detail the morphology of the subducted slabs associated with the Izanagi and India plates. We observe that in all models, although hampered for very strong plates and a layered mantle, the slabs exhibit a reciprocal dynamic attraction, clearly induced by a "hydrodynamic" effect involving mantle flow. The effect on the surface, on trench migration, of this interaction is the symmetry of the spins (rotations) of the two plates, rotating India in clockwise direction, while Izanagi in anti-clockwise direction. We suggest that these rotations are responsible of the symmetry observed in the hot spot tracks (Pacific) and fracture zone bends (Indian plate) observed for the period 120–80 Ma. This is discussed more in depth in the next section.

5. Discussion

[44] Several studies have been carried out focusing on the interaction between global mantle flow and plate tectonics, assuming a knowledge of the kinematic history on the Earth surface, either studying the feedback between mantle flow and plate motion [*Lithgow-Bertelloni and Richards*, 1998] or parameterizing slab pull as plate boundary force [*Conrad and Lithgow-Bertelloni*, 2002] or through a search through a set of rheological parameters aiming at the best fitting of observed kinematics [*Stadler et al.*, 2010]. Most global models rely on physically simpler rheologies than regional ones. Furthermore, regional models allow higher resolutions, which in turn facilitate an analysis of the effect of sharp material transitions such as in proximity of a subducting slab. Global models, however, have offered a great opportunity for testing geological hypothesis [*Jiménez-Munt and Platt*, 2006; *Bunge and Grand*, 2000], plate reconstructions [*Steinberger et al.*, 2004], the causes of the present lithospheric stress state [*Lithgow-Bertelloni and Guynn*, 2004], or for attempting a statistical

Geochemistry Geophysics Geosystems G3 10.1029/2011GC003843

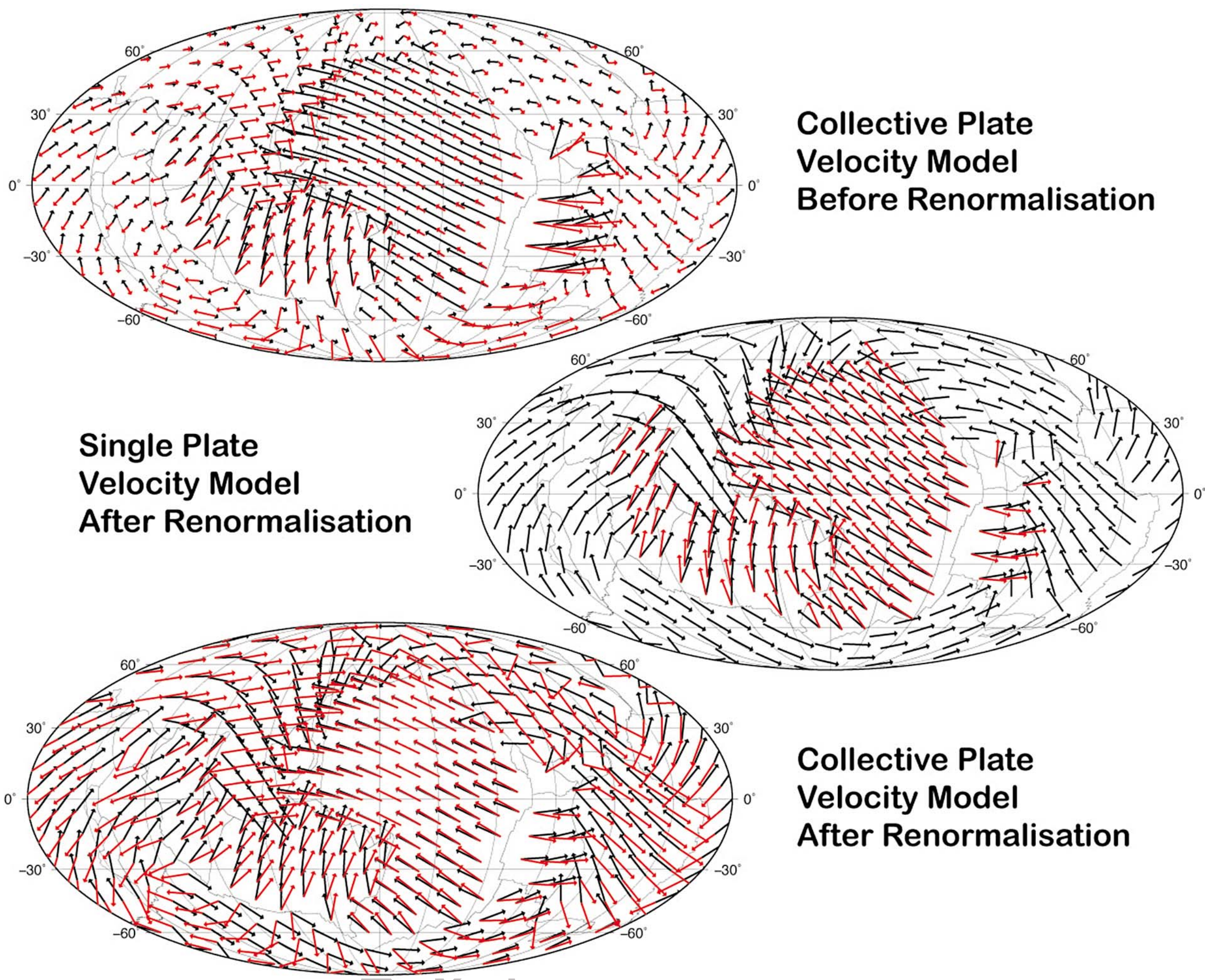

Figure 10. Comparison of the models of about 100 Ma, subduction of Izanagi and India, in the period around 100 Ma. We compared the single plate subduction (green) with the coupled model (yellow) for 4 configurations characterized by either a strongly layered mantle, or a homogeneous mantle, and a plate viscosity either 200 times the upper mantle, or 500 times. We argue that this plate rotation was responsible for the slow rotation of Indian plate and Izanagi plate (now evident only in the hot spot bend in the Pacific plate) that characterizes the 100 Ma plate reorganization.

global analysis of the regional behavior of each subduction zone [*Heuret et al.*, 2007; *Schellart et al.*, 2008]. Yet, these results have left undisclosed much about the physical nature of plate tectonics, either due to the use of imposed kinematic reconstructions as boundary conditions [*Han and Gurnis*, 1999] or due to approximated implementation of subduction zones [*Conrad and Lithgow-Bertelloni*, 2002].

[45] Our methodological approach is based on particularly simplified assumptions for lithosphere and mantle rheologies, i.e., a linear viscosity for each domain. Although this is a major assumption compared to the complications of the physics of tectonics, this "mean-field" approach has the advantage to lead to an understanding of the meaning of the few observables that are available from plate reconstructions, without the need of excessive parameter fitting. In fact our simple setup is easily interpreted in physical terms, and the origin of the discrepancies between our models and kinematic models indicate the presence and importance of finer tectonic details. Based on this approach four main interpretations of our models are proposed here.

5.1. Plate Fragmentation

[46] The reconstruction of plate boundaries in the past 200 Myr shows that there are strong regularities in size and shapes of the tectonic plates,

however the origin of the size and morphology of such plates is in many ways mysterious. Several authors have emphasized that there are two plate categories, one composed of "large" plates, whose size is of the same order of mantle thickness, and a second composed of "small" plates, whose size is much smaller than any convective cell [*Anderson*, 2002; *Bird*, 2003; *Sornette and Pisarenko*, 2003]. The rectangular plate models, having sizes varying between 0.5 and 2 times R_{Earth}, belong to the first category.

[47] We have calculated the local plateness of each rectangular plate and shown that it displays a peak at around $L_{litho} = R_{Earth}$. The existence of such general patterns has been confirmed by the superposition of the results of the models of plates with different width (Figure 5), and different plate viscosity (Figure 6). We find that the stability of plateness for plate lengths below two times mantle thickness and the decay for greater lengths is associated with a change in the plate mantle coupling. In detail, when the plate is no longer than 6000 km, the advective flow induced by the sinking slab generates a uniform drag below the plate, like a channel, therefore the plate moves faster and uniformly, inducing the maximum plateness. For greater lengths, instead, the induced flow from the sinking plate induces a smaller convective cells compared to the plate length, and therefore the drag below the plate opposes the plate motion, inducing the observed decay in plate velocity and plateness (Figure 5).

[48] While the amount of decay of plateness might rescale with the addition of a LVZ at the base of each plate, necessary to justify the high velocities of the Pacific plate, the basal friction at the base of the plate maintains its proportionality with plate length L_{litho}. We therefore argue that there exists a natural length scale for the size of the plate, which is about two times the mantle thickness $L_{litho} = R_{Earth}$. This result is an agreement with the statistical evidence that plate size for the greatest 6–8 plates is approximately this value [*Anderson*, 2002; *Bird*, 2003]. Furthermore this agrees with the observed plate fragmentation in the last 200 Myr, i.e., after the breakup of Pangea. In fact, while continental breakup is due to the rifting followed by a ridge formation, the rupture of an oceanic plate is a rare event, related to different conditions: plate reconstructions show that the all the episodes of fragmentation of an oceanic plate have happened in what is presently the Pacific Ocean. We argue that this has happened because only in this basin the critical plate size, R_{Earth}, has been reached.

[49] In more detail, the appearance of mid ocean ridges in oceanic plates can be fundamentally grouped in two categories, one in which a plate fragments through the appearance of a ridge normal to the trench (e.g., Kula from Farallon) or parallel to the trench (e.g., the ridges that appear in the Indian plate between 140 and 100 Ma). If we assume that the main force driving plates is slab pull, we find that the first category of new ridges appears parallel to the main stress direction, while the second appears normal to it. The plot showing the distribution of plateness in our models offers a key to explain both phenomena:

1. If a plate is very short (in length) but very wide, strong mantle layering will induce folding of the trench as shown in Figure 7, triggering opposing advancing and retreating trench migration and inducing lateral tensile stresses by the difficulty to maintain plate rigidity due to the Earth sphericity for plates width W_{litho} above R_{Earth}. Such behavior has been already observed in mud and other tensile stress dominated fracture systems [*Sammis and Ben-Zion*, 2008; *Bonnet et al.*, 2001].

2. If a plate is very long, beyond the critical length $L_{litho} = R_{Earth}$, the motion of the mantle does not sustain the plate's motion, and the drag below the plate will induce the system toward naturally developing a new trench-parallel ridge at that critical distance; an examples of this kind of fragmentation is the appearance of the Indian plate around 125 Ma, but also the appearance of the three ridges bounding the Pacific plate at its inception, and possibly even the breakup of the African from the South American one.

[50] The only exception to this scenario is the present Pacific plate, which reached its maximum size at around 55 Ma, and whose size is still beyond the critical values we find. We propose two possible explanations for this anomaly. The first is based on several lines of evidence suggesting that the Pacific plate is in the process of breaking up. These are the observation of an increasing distance between key fracture zones [*Goodwillie and Parsons*, 1992] and the emplacement of volcanic ridges without age progression along a possible lithospheric crack [*Sandwell et al.*, 1995]. Although such volcanic ridges may also indicate the presence of small scale convection at the base of the plate [*Ballmer et al.*,

2007], their orientation and regularity is always stimulated by an extensional regime, as predicted by our model (Figure 7). This interpretation has been recently disputed [*Forsyth et al.*, 2006] based on the lack of observations of faulting or graben formation; however, given that our model predicts a slow decrease of plate-mantle coupling, and consequently a very broad region of elastic stresses, this might help in reconciling the two interpretations.

[51] A second scenario emerges from the possibility that our assumption of full lithosphere-mantle coupling is incorrect. Numerical models of spontaneous plate tectonics advocate for the necessity of a plate-mantle decoupling, probably due to a low-viscosity zone at the base of the plates, to fit the observed poloidal-toroidal ratio of reconstructed plate velocities [*Tackley*, 2000a]. Our rectangular models show that the only plate for which such plate-mantle decoupling is required is the Pacific one, since otherwise its high plate velocity cannot be justified (Figure 8). As we will explain in the next section, such decoupling is not required for smaller plates.

5.2. Strong or Weak Plate-Mantle Coupling

[52] The main observation arising from the rectangular plate models of subduction in a homogeneous mantle ($\lambda = 1$) is that for equivalent slab pull (all models have an equally long and thick slab attached to the plate), the length of the plates (end to the trench distance) determines the speed of subduction if L_{litho} is above the value R_{Earth}. Below this length the slab pull uniquely determines the plate speed, as already shown in many numerical models [*Funiciello et al.*, 2003b; *Schellart*, 2005; *Stegman et al.*, 2006; *Capitanio et al.*, 2007; *Loiselet et al.*, 2009] and also fitting quite well natural observations [*Goes et al.*, 2008]. We refine the geodynamic models that require a viscous decoupling between mantle and plate [*Becker*, 2006; *Tackley*, 2000a], and we find that a low-viscosity zone is only necessary at the base of the Pacific plate and not for all the other oceanic plates, which have sizes below or close to R_{Earth}. This result is at odds with *Conrad and Lithgow-Bertelloni* [2002], who emphasize the role of the slab pull in controlling plate motion, but does not require a low-viscosity zone below the Pacific plate as we instead do.

[53] We have chosen to consider Euler stage poles orientation, i.e., the direction of plate motion and not its magnitude, as the former is controlled by the chosen 1-D profile of the mantle [*Goes et al.*, 2008; *Cammarano et al.*, 2010], due to the predominance of the dissipation in the mantle during the subduction process. Because the 1-D profile is still largely unknown, we believe that plate motion direction can be simply obtained from modeling slab pull and from the influence of slab-slab interaction, at least for the largest plates. At smaller scales, we believe that the inter-plate interaction will be more important, in particular through a complex time-dependent and strongly varying regional evolution.

[54] The results of rectangular and global reconstructed plate models show that taking account of the entire tectonic tessellation is essential to obtain a proper representation of the flow within the plate-mantle system. We want to stress that this is not in contradiction with the subduction models that have emphasized the role of the 660 km discontinuity. It is well-supported by mantle tomography that all the large slabs above a critical size (several times wider of 600 km, as all the ones that we have modeled here) have actually crossed the upper-lower mantle discontinuity, even when the timing and mechanism of this process is only partially understood [*Goes et al.*, 2008]. We therefore modeled only the largest scale flow, which is responsible of linking the regional with the global scale. Further research is necessary to model the details of the regional scale, such as the trench migration and the interaction of the slab with a complex transition zone.

5.3. The "100 Ma" Plate Reorganization

[55] While the well known plate reorganization associated with the 50 Ma bend of hot spots tracks such as the Hawaii-Emperor seamount chain has been intensively investigated [*Whittaker et al.*, 2007; *Tarduno et al.*, 2009], the other major global plate reorganization that characterizes the last 200 Myr, has received less attention. This event happened approximately during the Cretaceous Normal Superchron (CNS) [*Wessel et al.*, 2006] at around 100 Ma and is therefore sometimes referred to as the "99 Ma" plate reorganization [*Veevers*, 2000]. A global analysis of the bends in fracture zones in the all ocean basins formed during the CNS (120–83 Ma), together with seafloor spreading rate estimates for ocean floor formed at that time, results in dating estimates ranging 3–8 Myr between four separate locations in the Indian Ocean where the bend is well expressed (K. Matthews et al., manuscript in preparation, 2012). In addition, the hot spot track bend around 100 Ma in the Pacific plate is much less distinct, suggesting that the reorganization started from an abrupt event involving

the Indian plate and propagated to Izanagi and the Pacific plates.

[56] While the slowness of the propagation of the reorganization from the regional to the global scale is in agreement with prior studies of mantle flow, which predict slow reorganization [*King et al.*, 2002], our models directly offer an explanation for the "globalization" of the event, which propagated from an initial event related to the Indian basin, to a following rotation of the Pacific plate. Starting from reconstructed geometries of 125 Ma, just before the 100 Ma reorganization begins, our models show that slabs attached to two large plates in the same hemisphere (India and Izanagi) interact through the induced mantle flow by the sinking of the associated slabs. Figures 9 and 10 show very clearly how this slab-slab coupling generates a lateral gradient of drag on the slabs themselves, inducing a toroidal movement on the surface of the attached plates, which corresponds to the estimated anti-clockwise rotation seen in the hot spot trace in the Pacific and to the simultaneous clockwise rotation of the fracture zones in the Indian plate.

[57] The observation of the broad Pacific hot spot track bend and of the narrow bend of the fracture zones in the Indian plate suggests that our mantle-mediated mechanism of propagation of reorganization offers both a justification of the different speed of the two rotations, which are otherwise perfectly coherent in direction and timing, and a general mechanism to understand how plate reorganizations, such as the one of 50 Ma, may become global, although initially originate regionally. Our models show that a "hydrodynamic" pull existed between the Indian and Izanagi plates assuming a sufficiently layered mantle (viscosity ratio of 5) and based on their reconstructed configuration (trenches facing each other. More tests are presented by G. Morra and F. Funiciello (manuscript in preparation, 2012). This attraction has likely played a leading role in the simultaneous reorganization of the two plates. It is however not clear yet which mechanism has triggering the initiation of the reorganization, possibly being the subduction of a ridge or a continent fragment.

6. Conclusions

[58] We show here how with a pure boundary element method based software, called "bemEarth," based on a fast multipole algorithm, we are able to solve the momentum equation and simulate the coupled regional-global geodynamics in a 3-D spherical setting. This approach is much faster then the classical finite difference and finite element methods, allows an easier implementation of a free surface, but can be very complex to implement. Special ad hoc formulations (see Appendix A) are also necessary for treating nonhomogeneous domains. We show that plate geometries and velocities at present and past times, extracted from plate reconstructions with the GPlates software, can be transformed into space domains with different densities and viscosities, which was in turn sufficient to create models for large-scale Earth evolution that overall match kinematically modeled plate velocities.

[59] An analysis of the subduction in an homogeneous mantle (λ = 1) of very large rectangular plates, with length and width varying between one and four times the mantle thickness, shows that when the plate size in the direction of convergence (L_{litho}) is below about Earth radius (R_{Earth}), the velocity of plate motion is completely driven by slab pull and the length of the plate plays a minor role, while for greater plates plate speed reduces dramatically, of over 50% for $L_{litho} = 2R_{Earth}$. Plate width instead exerts little influence on plate speed. An analysis of the mantle flow induced by the plate subduction shows that this effect is related to the size of the induced cell in the mantle, and that above this threshold mantle flow opposes plate advancing, while below it the slab induced mantle flow accommodates plate motion.

[60] We observe that the pattern described above is interrupted when mantle layering is strong enough. For λ = 10 and above, the plateness decays strongly with mantle layering, indicating a lateral heterogeneous behavior (Figure 6). Furthermore for a strongly layered mantle very wide plates display lateral folding along the trench and naturally both trench retreat and advance, in accordance with the results of *Stegman et al.* [2006], and trench advance for very strong plates (viscosity above 500). This result suggests that the subduction of very wide plates in a strongly layered mantle is characterized by fast opening and closing of back-arc basins. In the long-term, any given slab penetrates into the lower mantle, possibly after buckling, and its slow sinking in the lower mantle then creates a slow flow described by the scenarios based on a homogeneous mantle, as for lower strain rates upper lower mantle decoupling is expected to be less intense.

[61] When translated into plotting local plateness, we therefore find that several mechanisms trigger low plateness conditions, which we interpret as

"tendency toward fragmentation." These results have implications for the origin and evolution of the sizes of the largest plates on the Earth: an oceanic plate will tend to fragment, opening a new mid-oceanic ridge, for sizes around $L_{litho} = W_{litho} = R_{Earth}$ in the direction of extension, either normal or parallel to the motion. Such results integrate well with the statistics of large plates arising from the plate statistics of the past 150 Myr (G. Morra et al., submitted manuscript, 2012).

[62] The application of our model to the large-scale reconstructed plate tessellation at 25 and 125 Ma shows how the pull due to the slabs derived only by plate history is able to reproduce most of the observed plate motion for the largest subducting plates, which are the fastest moving plates on the Earth, although a low-viscosity zone is required to justify the high velocities of the Pacific plate.

[63] The models starting from the 125 Ma configuration offer new insights into the nature of the global plate reorganization at ~100 Ma. The deep mantle interaction between the subducting slabs of the Indian and Izanagi plates is able to transmit the reorganization of the Indian plate to the Izanagi and Pacific plates. The interaction between the slabs can have also driven the system toward instability, through a hydrodynamic attraction between the two sinking slabs, as common in low Reynolds number hydrodynamic [*Manga and Stone*, 1995].

Appendix A: Approximated Boundary Integrals for Nonhomogeneous Fluids

[64] We show in this appendix first how to obtain equation (4), then how we perturbed it to consider the nonhomogeneous radial profile and finally how we estimate the associated error. The original integral equation obtained by *Ladyzhenskaya* [1963]

$$u_i(\mathbf{x}) + \frac{1}{8\pi}\int_{\partial D} T_{ijk}(\mathbf{x},\mathbf{x}_o)u_j(\mathbf{x})n_k(\mathbf{x})dS(\mathbf{x}) = -\frac{1}{8\pi\mu}\int_{\partial D} G_{ij}(\mathbf{x},\mathbf{x}_o)\sigma_{jk}(\mathbf{x})n_k(\mathbf{x})dS(\mathbf{x}) \quad \text{(A1)}$$

represents the velocity $u(\boldsymbol{x})$ for each point $\boldsymbol{x}$ inside the domain $\boldsymbol{D}$, where the viscosity is μ. The integral is calculated only on the boundary $\partial\boldsymbol{D}$. Ladyzhenskaya has shown that $u(\boldsymbol{x}) = 0$ when $x \notin \boldsymbol{D}$.

[65] If we define the viscosity outside the domain $\boldsymbol{D}$ as $\lambda\mu$, we can rewrite the equation (1) inside and outside $\partial\boldsymbol{D}$, respectively, and take all the integrals at the right hand side, to facilitate their manipulation. We stress that the normal is always toward outside $\partial\boldsymbol{D}$:

$$\begin{aligned} u_i(\mathbf{x}) &= -\frac{1}{8\pi\mu}\int_{\partial D} G_{ij}(\mathbf{x},\mathbf{x}_o)\sigma_{jk}(\mathbf{x})n_k(x)dS(\mathbf{x}) \\ &\quad -\frac{1}{8\pi}\int_{\partial D} T_{ijk}(\mathbf{x},\mathbf{x}_o)u_j(\mathbf{x})n_k(\mathbf{x})dS(\mathbf{x}) \\ u_i(\mathbf{x}) &= \frac{1}{8\pi\lambda\mu}\int_{\partial D} G_{ij}(\mathbf{x},\mathbf{x}_o)\sigma_{jk}(\mathbf{x})n_k(\mathbf{x})dS(\mathbf{x}) \\ &\quad +\frac{1}{8\pi}\int_{\partial D} T_{ijk}(\mathbf{x},\mathbf{x}_o)u_j(\mathbf{x})n_k(\mathbf{x})dS(\mathbf{x}) \end{aligned}$$

where $\boldsymbol{x_o}$ indicates a different point for the two equations. If we let $\boldsymbol{x_o}$ collapsing on the boundary $\partial\boldsymbol{D}$, *Ladyzhenskaya* [1963, p. 75] shows that when $x \notin \partial\boldsymbol{D}$ a limit (jump) condition can be established and the two above equations become (see also *Pozrikidis* [1992, chap. 3] for a rigorous demonstration)

$$\begin{aligned} \frac{1}{2}u_i(\mathbf{x}) &= -\frac{1}{8\pi\mu}\int_{\partial D} G_{ij}(\mathbf{x},\mathbf{x}_o)\sigma_{jk}(\mathbf{x})n_k(\mathbf{x})dS(\mathbf{x}) \\ &\quad -\frac{1}{8\pi}\int_{\partial D} T_{ijk}(\mathbf{x},\mathbf{x}_o)u_j(\mathbf{x})n_k(\mathbf{x})dS(\mathbf{x}) \\ \frac{1}{2}u_i(\mathbf{x}) &= \frac{1}{8\pi\lambda\mu}\int_{\partial D} G_{ij}(\mathbf{x},\mathbf{x}_o)\sigma_{jk}(\mathbf{x})n_k(\mathbf{x})dS(\mathbf{x}) \\ &\quad +\frac{1}{8\pi}\int_{\partial D} T_{ijk}(\mathbf{x},\mathbf{x}_o)u_j(\mathbf{x})n_k(\mathbf{x})dS(\mathbf{x}) \end{aligned}$$

now $\boldsymbol{x_o}$ coincides for both equations, hence combining them linearly (see *Rallison and Acrivos* [1978, equations (3)–(8)] for even more details) we obtain

$$\frac{1+\lambda}{2}u_j(\mathbf{x}_o) = \frac{1}{8\pi\mu}\int_{\partial D}\Delta f_i(\mathbf{x})G_{ij}(\mathbf{x},\mathbf{x}_o)dS(\mathbf{x}) - \frac{1-\lambda}{8\pi}\int_{\partial D} u_i(\mathbf{x})n_k^{out}(\mathbf{x})T_{ijk}(\mathbf{x},\mathbf{x}_o)dS(\mathbf{x}) \quad \text{(A2)}$$

where the double layer appears only when the viscosity inside and outside $\partial\boldsymbol{D}$ is different. Δf_i represents the jump in the traction between inside and outside the boundary:

$$\begin{aligned} \Delta f_i(\mathbf{x}) &= \sigma_{ik}^{out}(\mathbf{x})n_k^{out}(\mathbf{x}) + \sigma_{ik}^{in}(\mathbf{x})n_k^{in}(\mathbf{x}) \\ &= \left[\sigma^{out}(\mathbf{x}) - \sigma_{ik}^{in}(\mathbf{x})\right]n_k^{out}(\mathbf{x}). \end{aligned}$$

[66] An extensive literature on how to extrapolate the differential traction at boundaries for fluid-dynamic systems exists. In this work we will only employ $\Delta f(\mathbf{x}) = \Delta\rho g \cdot \mathbf{x}n_i^{out}(\mathbf{x})$ defining the gravity

potential (more details can be found in the work of *Pozrikidis* [1992]).

[67] In this work a perturbed formulation of equation (A2) is adopted, in order to approximate to effect of a nonhomogeneous background viscosity, as shown in Figure 1a for a subducting slab through the upper-lower mantle. The new formulation can be obtained multiplying equation (A1) for the viscosity μ and take the viscosity inside the double layer integral:

$$\mu u_i(\mathbf{x}) + \frac{1}{8\pi}\int_{\partial D} \mu T_{ijk}(\mathbf{x},\mathbf{x}_o)u_j(x)n_k(\mathbf{x})dS(\mathbf{x}) = -\frac{1}{8\pi}\int_{\partial D} G_{ij}(\mathbf{x},\mathbf{x}_o)\sigma_{jk}(\mathbf{x})n_k(\mathbf{x})dS(\mathbf{x}) \quad \text{(A3)}$$

This formulation has a natural interpretation: the viscosity is multiplied to the "target" velocity in the first term of the RHS, while it is associated with the "source" velocity inside the integral of the second term of the RHS. It is therefore natural to consider the "natural extension" of the Boundary Integral Equations for a nonhomogeneous fluid whose viscosity is expressed as $\mu(\boldsymbol{x})$:

$$\mu(\mathbf{x})u_i(\mathbf{x}) + \frac{1}{8\pi}\int_{\partial D} \mu(\mathbf{x}) T_{ijk}(\mathbf{x},\mathbf{x}_o)u_j(\mathbf{x})n_k(\mathbf{x})dS(\mathbf{x}) = -\frac{1}{8\pi}\int_{\partial D} G_{ij}(\mathbf{x},x_o)\sigma_{jk}(\mathbf{x})n_k(\mathbf{x})dS(\mathbf{x}) \quad \text{(A4)}$$

Clearly very refined heterogenities will require the full integration of the involved volume. In fact we apply this approach only to the system displayed in Figure 1, characterized by a viscosity increase from upper to lower mantle (from now on called μ_1 and μ_2, with $\mu_2 > \mu_1$), and μ_{litho} for the viscosity inside the subducting plate.

[68] Following now the same procedure used to obtain equations (A2) and (A4) can be written for the domain inside and outside ∂D and considering that the first term becomes 1/2 $u(\boldsymbol{x})$ when $\boldsymbol{x}$ lies on the surface ∂D and calling $\gamma = \mu_2/\mu_1$

$$\frac{1}{2}u_i(\mathbf{x}) + \frac{1}{8\pi}\int_{\partial D_1} T_{ijk}(\mathbf{x},\mathbf{x}_o)u_j(\mathbf{x})n_k(\mathbf{x})dS(\mathbf{x}) + \frac{\gamma}{8\pi}\int_{\partial D_2} T_{ijk}(\mathbf{x},\mathbf{x}_o)u_j(\mathbf{x})n_k(\mathbf{x})dS(\mathbf{x}) = -\frac{1}{8\pi\mu_1}\int_{\partial D} G_{ij}(\mathbf{x},\mathbf{x}_o)\sigma_{jk}(\mathbf{x})n_k(\mathbf{x})dS(\mathbf{x}) \quad \text{(A5)}$$

for every x belonging to ∂D_1 (upper mantle in Figure 1) and

$$\frac{1}{2}\gamma u_i(\mathbf{x}) + \frac{1}{8\pi}\int_{\partial D_1} T_{ijk}(\mathbf{x},\mathbf{x}_o)u_j(\mathbf{x})n_k(\mathbf{x})dS(\mathbf{x}) + \frac{\gamma}{8\pi}\int_{\partial D_2} T_{ijk}(\mathbf{x},\mathbf{x}_o)u_j(\mathbf{x})n_k(\mathbf{x})dS(\mathbf{x}) = -\frac{1}{8\pi\mu_1}\int_{\partial D} G_{ij}(\mathbf{x},\mathbf{x}_o)\sigma_{jk}(\mathbf{x})n_k(\mathbf{x})dS(\mathbf{x}) \quad \text{(A6)}$$

for every $\boldsymbol{x}$ belonging to ∂D_2 (lower mantle in Figure 1).

[69] For the same integral inside the slab, and defining $\xi = \mu_{litho}/\mu_1$, we get for every $\boldsymbol{x}$ on ∂D_1 that

$$\frac{1}{2}\xi u_i(\mathbf{x}) - \frac{\xi}{8\pi}\int_{\partial D_1 \cup \partial D_2} T_{ijk}(\mathbf{x},\mathbf{x}_o)u_j(\mathbf{x})n_k(\mathbf{x})dS(\mathbf{x}) = -\frac{1}{8\pi\mu_1}\int_{\partial D} G_{ij}(\mathbf{x},x_o)\sigma_{jk}(\mathbf{x})n_k(\mathbf{x})dS(\mathbf{x}) \quad \text{(A7)}$$

and for every $\boldsymbol{x}$ on ∂D_2 (slab in the lower mantle in Figure 1)

$$\frac{1}{2}\xi u_i(\mathbf{x}) - \frac{\xi}{8\pi}\int_{\partial D_1 \cup \partial D_2} T_{ijk}(\mathbf{x},\mathbf{x}_o)u_j(\mathbf{x})n_k(\mathbf{x})dS(\mathbf{x}) = -\frac{1}{8\pi\mu_1}\int_{\partial D} G_{ij}(\mathbf{x},\mathbf{x}_o)\sigma_{jk}(\mathbf{x})n_k(\mathbf{x})dS(\mathbf{x}) \quad \text{(A8)}$$

combining now linearly equations (A5) and (A7) in ∂D_1 and equations (A6) and (A8) in ∂D_2, we obtain the final set of equations, respectively

$$\frac{1}{2}(1+\lambda)u_i(\mathbf{x}) + \frac{1-\lambda}{8\pi}\int_{\partial D_1} T_{ijk}(\mathbf{x},\mathbf{x}_o)u_j(\mathbf{x})n_k(\mathbf{x})dS(\mathbf{x}) + \frac{\gamma-\lambda}{8\pi}\int_{\partial D_2} T_{ijk}(\mathbf{x},\mathbf{x}_o)u_j(\mathbf{x})n_k(\mathbf{x})dS(\mathbf{x}) = -\frac{1}{8\pi\mu_1}\int_{\partial D} G_{ij}(\mathbf{x},\mathbf{x}_o)\sigma_{jk}(\mathbf{x})n_k(\mathbf{x})dS(\mathbf{x}) \quad \text{(A9)}$$

$$\frac{1}{2}\gamma(1+\lambda)u_i(\mathbf{x}) + \frac{1-\lambda}{8\pi}\int_{\partial D_1} T_{ijk}(\mathbf{x},\mathbf{x}_o)u_j(\mathbf{x})n_k(\mathbf{x})dS(\mathbf{x}) + \frac{\gamma-\lambda}{8\pi}\int_{\partial D_2} T_{ijk}(\mathbf{x},\mathbf{x}_o)u_j(\mathbf{x})n_k(\mathbf{x})dS(\mathbf{x}) = -\frac{1}{8\pi\mu_1}\int_{\partial D} G_{ij}(\mathbf{x},\mathbf{x}_o)\sigma_{jk}(\mathbf{x})n_k(\mathbf{x})dS(\mathbf{x}) \quad \text{(A10)}$$

Examples of the effects of the upper lower mantle viscosity ratio are represented in Figure A1. In order to understand how the boundary element

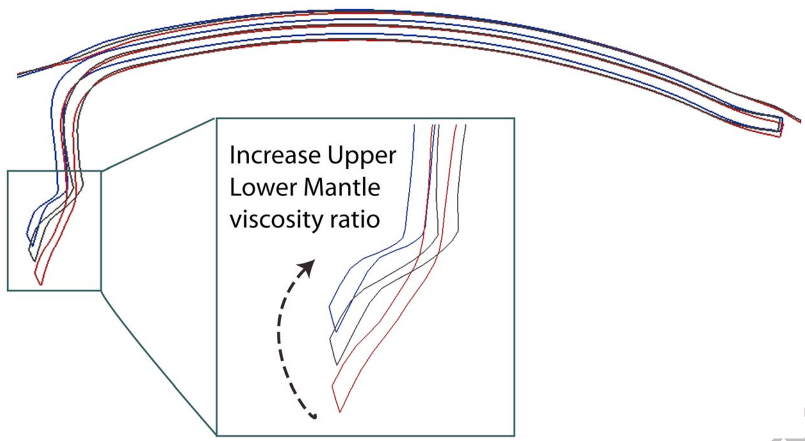

Figure A1. Comparison of three subduction models using the same setup of Figure D1, but varying the upper-lower mantle viscosity ratio with the implementation illustrated in Appendix A.

method represents the far transmission of stress between different domains, like the slab immersed in the upper mantle, or in the lower mantle, it is here instructive to analyze how equations (A9) and (A10) simplify for the simple case of two different viscosities, one for the upper and one for the lower mantle (Figure 1). Natural values for ξ and γ from the literature are 100–500 and 10–30, respectively. Exploiting that at the first order $(1 + \xi) \cong \xi$, $(1 - \xi)/(1 + \xi) \cong -1 + 2/\xi \cong 1$ and $(\gamma - \xi)/(1 + \xi) \cong -1 + \gamma/\xi$ for large values of γ and $\gamma > \xi$, equations (A9) and (A10) collapse, respectively, into

$$\frac{1}{2}u_i(\mathbf{x}) - \frac{1}{8\pi}\int_{\partial D_1} T_{ijk}(\mathbf{x},\mathbf{x}_o)u_j(\mathbf{x})n_k(\mathbf{x})dS(\mathbf{x}) - \frac{1-\gamma/\lambda}{8\pi}\int_{\partial D_2} T_{ijk}(\mathbf{x},\mathbf{x}_o)u_j(\mathbf{x})n_k(\mathbf{x})dS(\mathbf{x}) = -\frac{1}{8\pi\mu_1(1+\lambda)}\int_{\partial D} G_{ij}(\mathbf{x},\mathbf{x}_o)\sigma_{jk}(\mathbf{x})n_k(\mathbf{x})dS(\mathbf{x}) \quad \text{(A11)}$$

$$\frac{1}{2}\gamma u_i(\mathbf{x}) - \frac{1}{8\pi}\int_{\partial D_1} T_{ijk}(\mathbf{x},\mathbf{x}_o)u_j(\mathbf{x})n_k(\mathbf{x})dS(\mathbf{x}) - \frac{1-\gamma/\lambda}{8\pi}\int_{\partial D_2} T_{ijk}(\mathbf{x},\mathbf{x}_o)u_j(\mathbf{x})n_k(\mathbf{x})dS(\mathbf{x}) = -\frac{1}{8\pi\mu_1(1+\lambda)}\int_{\partial D} G_{ij}(\mathbf{x},\mathbf{x}_o)\sigma_{jk}(\mathbf{x})n_k(\mathbf{x})dS(\mathbf{x}) \quad \text{(A12)}$$

from which it is possible to observe that the propagation of the stress from the lower mantle to the slab in upper mantle is taken by the γ/ξ in the second integral of the LHS, which means that weaker slabs will be more affected, although this effect is so small that it is probably not detectable. If the equations were decoupled, the sinking velocity for a slab in the lower mantle, for equivalent geometry, would be proportional to the lower/upper mantle viscosity ratio, and divergent solutions from that derive from the coupling between the two equations.

Appendix B: Resolution Test for the Subduction of a Squared 6000 × 6000 km Plate

[70] Figure B1 shows the outcome of 6 resolution tests on a plate of size $R_{Earth} \times R_{Earth}$, subducting in a homogeneous mantle, with the same conditions of the rectangular models analyzed in this work. We varied the element length from $L_{max} = (1/0.75) \cdot 10^{-2} \cdot R_{Earth}$ to $L_{max} = (1/2.00) \cdot 10^{-2} \cdot R_{Earth}$, corresponding to 5625 and 40,000 panels, respectively. The outcomes displayed in Figure B1 are sections of the 3-D simulations, after 100 time steps. The displayed evolution of the surface geometry is defined by a second-order Runge-Kutta advection scheme applied to the vertices of the boundary elements. The results show the convergence of the results toward a solution, which confirms the stability of the approach for the setup employed in this work (free surface, lubrication approach for the motion of the lithosphere). The main difference between highly resolved and less resolved slabs is a higher flexibility of the best models, visible in the deformation of the trench and the tip of the subducting slab. We cannot benchmark such a complicate system with an analytical solution, however we observe how the correction due to the increase of the resolution becomes less at higher resolution, suggesting convergence to a final solution. It is important for the calculation of plateness to observe that the stretching of the "still

10.1029/2011GC003843

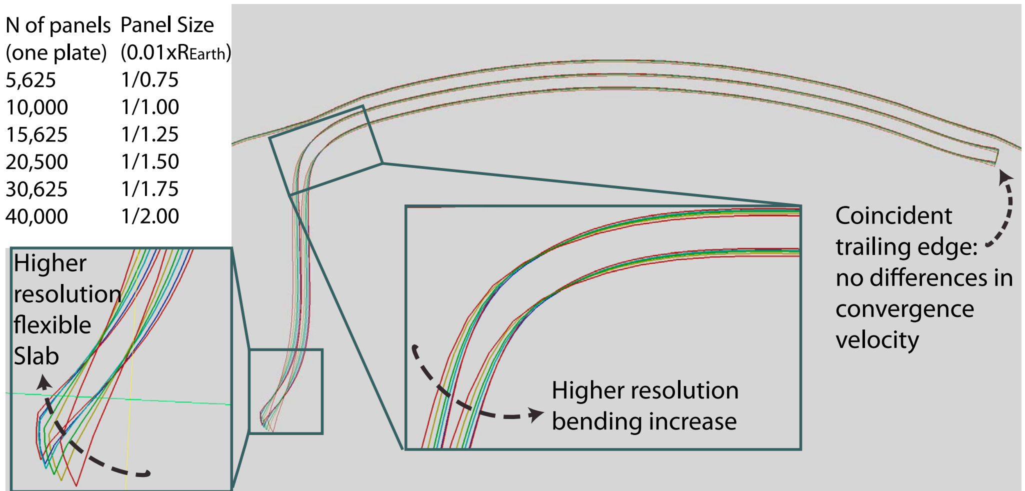

Figure B1. Resolution test for the same standard model of Figure D1. The finer the resolution, the more is the slab flexible. For sufficiently high resolution, the model converges toward the same solution.

unsubducted" plate and the resulting position of the trailing edge, are little or no affected by variation of plate mesh resolution.

Appendix C: Benchmark of the Role of the Viscosity of the Downgoing Plate

[71] In order to test the role of viscosity we tested the same configuration of Appendix C (squared plate sized $R_{Earth} \times R_{Earth}$, subducting in an homogeneous mantle), comparing two slab viscosities: 100 and 200 times higher of the mantle viscosity (Figure C1). Coherently with other analog and numerical models [*Funiciello et al.*, 2003b; *Schellart*, 2005; *Stegman et al.*, 2006; *Capitanio et al.*, 2007; *Goes et al.*, 2008; *Ribe*, 2010; *Stegman et al.*, 2010b], we do not observe any effect of the plate viscosity to subduction speed, implying a minimum amount of viscous dissipation inside the slab, compared to the mantle creep. Another important observation is the minimum amount of variation of plate deformation of the unsubducted plate, indicating similar plateness. Finally as expected, and coherently with analog and numerical models, we observe a weakening and increase in stretching for a less viscous slab. The difference between the 100x and 200× model is an increase in stretching is between 5% and 10% after 100 time steps. The morphology of the slab is highly

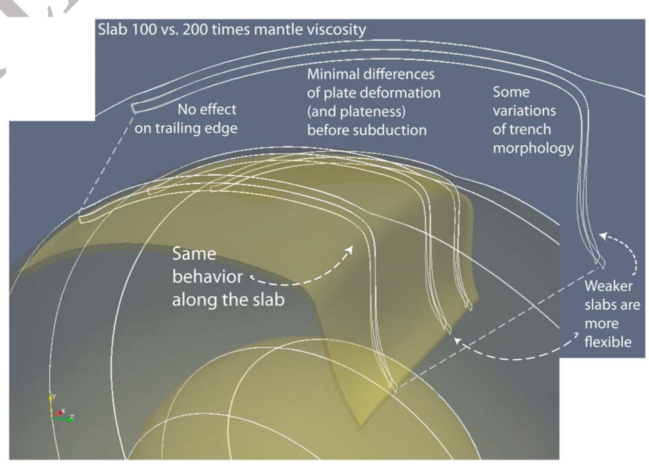

Figure C1. Comparison between a highly viscous (200 times the mantle viscosity) and low-viscous (100 times) slab. The plate motion is almost identical as indicated by the fixed plate trail, while the slab edge is much more flexible and stretched in the low-viscous case.

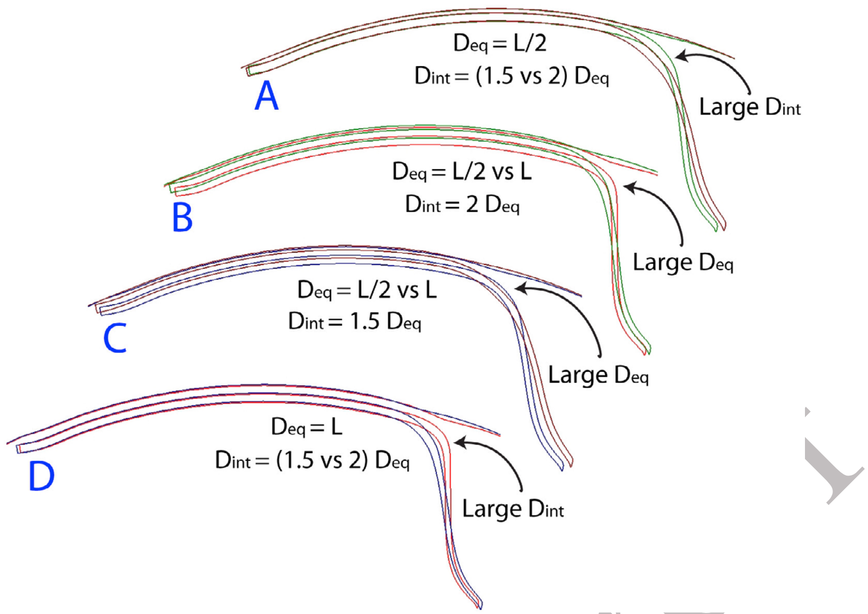

Figure D1. Exploration of four setups relative to the implementation of the free surface for the same subduction system. D_{eq} (equilibrium distance) is varied between L/2 and L, while D_{int} is varied relatively to D_{eq}: from 1.5 D_{eq} to 2 D_{eq}.

compatible with the results predicted by *Ribe* [2001].

Appendix D: Contact Algorithm and Free Surface

[72] The implementation of the free surface, the same as in the work of *Morra et al.* [2009] to which we redirect for more details, is relatively complex, and its goal is to "adapt" the free surface delimiting the mantle to the subducting plate, but allowing the plate to detach from the surface in order to subduct. In order to achieve this goal the method is based on the adaptation of the external surface (defining the Earth surface) to the subducting slab, using a "master-slave" algorithm. In detail, the vertices of the elements of the Earth surface adapt to an "equilibrium" or "lubrication" distance from the subducting slab. In this way the slab can freely change its morphology, but when it deflects down, also the external surface follows it, spontaneously producing a restoring force counterbalancing buoyancy and leading the slab to equilibrium, achieving a perfectly equivalent formulation to a true free surface. This algorithm in detail works in the following way: (1) for each vertex of the external surface the closest element of plate is detected; (2) if the node of the surface is closer of a "critical interaction distance" called D_{int}, the "vertex-element centroid" vector is projected along the normal of the element in order to obtain the surface-surface distance; (3) the node of the surface is then displaced so that the projected distance is equal to the "equilibrium," or "lubrication," distance, here called D_{eq}. The algorithm is therefore based on two parameters: D_{int} and D_{eq}, where the first is always larger to the second. In detail the algorithm is synthesized in the following pseudo-code where panels. centroids refer to the elements (panels) of the "master surface" and nodes.coordinates indicate the positions of the vertices of the mesh of the "slave surface." This algorithm is always adopted assuming (1) the lithosphere as "master" and the Earth surface as "slave," (2) the overriding plate as "slave" and the downgoing plate as "master," and (3) the core as slave and the sinking slab as master:

```
differenceVector = nodes.coordinates[slave surface] - panels.centroids[master surface]);

distance = sqrt(innerproduct(differenceVector, differenceVector));

if (distance < D_int) then
{
normalDistance = innerproduct(differenceVector, panels.normals[master surface]);
```

```
if (normalDistance < D_eq)
{
distanceIncrease = D_eq - normalDistance; nodes.
coordinates[slave surface] + = distanceIncrease *
panels.normals[master surface]);
}
}
```

[73] As it has been shown in the work of *Schmeling et al.* [2008], comparing a large number of numerical and laboratory experiments, the formulation of the free surface can substantially change the morphology of the trench and the trench migration kinematics. We confirm this result, and show that not only the presence of a free surface, but also its implementation sensibly influences trench migration. In order to show this we varied D_{eq} and D_{int}, the first testing two values L and L/2 (where L is the thickness of the lithosphere), and comparing also the values of D_{int} 1.5 and 2 times D_{eq}. Several results emerge. The first is that, after 100 time steps (Figure D1), the formulation of the free surface does not vary either the position of the trailing edge or the plateness of the slab. However, the position of the trench, its morphology and therefore the shape of the subducted slab visibly change. In general a simple rule applies: (1) fixed D_{eq}, at greater values of D_{int} the trench retreat is more hampered, inducing smaller radius of curvature and more vertical slab dips, and (2) given D_{int}, a greater D_{eq} opposes trench retreat and induces more vertical dips.

[74] For the purpose of this paper, we observe that trench retreats are naturally highly dependent from the chosen free surface formulation. Very likely the presence of an upper plate will stabilize the unstable patterns that we display in Figure D1, as suggested by *Capitanio et al.*, 2010]. However, given that the subduction of plates whose overriding plate is a very thin back arc basin are very common, we suggest that 3-D complex plate migration mechanisms as suggested in Figure 7 are also very common. In this work we choose D_{int} and D_{eq} in order to hamper trench migration and in order to concentrate our study to plate motion and plateness for very stable trenches, as the ones of the large plates are.

Acknowledgments

[75] The authors would like to thank the Australian Research Council for financial support (DP0986377). G.M. thanks the Swiss National Science Foundation for financial support (Advanced Researcher Fellowship PA0022–121475) and the support by the Korea government (MEST, 2009–0092790). R.D.M. thanks the Australian Research Council for financial support (Laureate Fellowship). We are thankful to Thorsten Becker, Boris Kaus, Dave Stegman, and an anonymous reviewer for their numerous and interesting contributions during the reviewing process.

References

Anderson, D. L. (2002), How many plates?, *Geology*, *30*(5), 411–414, doi:10.1130/0091-7613(2002)030<0411:HMP>2.0.CO;2.

Artemieva, M. I. (2006), Global 1° × 1° thermal model TC1 for the continental lithosphere: Implications for lithosphere secular evolution, *Tectonophysics*, *416*(1–4), 245–277.

Ballmer, M. D., J. van Hunen, G. Ito, P. J. Tackley, and T. A. Bianco (2007), Non-hotspot volcano chains originating from small-scale sublithospheric convection, *Geophys. Res. Lett.*, *34*, L23310, doi:10.1029/2007GL031636.

Barnes, J., and P. Hut (1986), A hierarchical *O*(*N* log *N*) force-calculation algorithm, *Nature*, *324*, 446–449, doi:10.1038/324446a0, doi:10.1038/324446a0.

Becker, T. W. (2006), On the effect of temperature and strain-rate dependent viscosity on global mantle flow, net rotation, and plate-driving forces, *Geophys. J. Int.*, *167*(2), 943–957, doi:10.1111/j.1365-246X.2006.03172.x.

Becker, T. W., C. Faccenna, R. J. O'Connell, and D. Giardini (1999), The development of slabs in the upper mantle: Insights from numerical and laboratory experiments, *J. Geophys. Res.*, *104*(B7), 15,207–15,226, doi:10.1029/1999JB900140.

Becker, T. W., and R. J. O'Connell (2001), Predicting plate velocities with mantle circulation models, *Geochem. Geophys. Geosyst.*, *2*(12), 1060, doi:10.1029/2001GC000171.

Bellahsen, N., C. Faccenna, and F. Funiciello (2005), Dynamics of subduction and plate motion in laboratory experiments: Insights into the "plate tectonics" behavior of the Earth, *J. Geophys. Res.*, *110*, B01401, doi:10.1029/2004JB002999.

Benedetti, I., M. H. Aliabadi, and G. Davì (2008), A fast 3D dual boundary element method based on hierarchical matrices, *Int. J. Solids Struct.*, *45*(7–8), 2355–2376, doi:10.1016/j.ijsolstr.2007.11.018.

Bercovici, D. (1998), Generation of plate tectonics from lithosphere-mantle flow and void-volatile self-lubrication, *Earth Planet. Sci. Lett.*, *154*, 139–151, doi:10.1016/S0012-821X(97)00182-9.

Bird, P. (2003), An updated digital model of plate boundaries, *Geochem. Geophys. Geosyst.*, *4*(3), 1027, doi:10.1029/2001GC000252.

Bonnet, E., O. Bour, N. E. Odling, P. Davy, I. Main, P. Cowie, and B. Berkowit (2001), Scaling of fracture systems in geological media, *Rev. Geophys.*, *39*(3), 347–383, doi:10.1029/1999RG000074.

Börm, S., L. Grasedyck, and W. Hackbusch (2003), Introduction to hierarchical matrices with applications, *Eng. Anal. Boundary Elem.*, *27*(5), 405–422, doi:10.1016/S0955-7997(02)00152-2.

Buffett, B. A., and A. Heuret (2011), Curvature of subducted lithosphere from earthquake locations in the Wadati-Benioff zone, *Geochem. Geophys. Geosyst.*, *12*, Q06010, doi:10.1029/2011GC003570.

Buffett, B. A., and D. B. Rowley (2006), Plate bending at subduction zones: Consequences for the direction of plate motions, *Earth Planet. Sci. Lett.*, *245*(1–2), 359–364, doi:10.1016/j.epsl.2006.03.011.

Buffett, B. A., C. W. Gable, and R. J. O'Connell (1994), Linear stability of a layered fluid with mobile surface plates, *J. Geophys. Res.*, *99*(B10), 19,885–19,900, doi:10.1029/94JB01556.

Bunge, H.-P., and S. P. Grand (2000), Mesozoic plate-motion history below the northeast Pacific Ocean from seismic images of the subducted Farallon slab, *Nature*, *405*(6784), 337–340, doi:10.1038/35012586.

Cammarano, F., H. Marquardt, S. Speziale, and P. J. Tackley (2010), Role of iron-spin transition in ferropericlase on seismic interpretation: A broad thermochemical transition in the mid mantle?, *Geophys. Res. Lett.*, *37*, L03308, doi:10.1029/2009GL041583.

Capitanio, F. A., G. Morra, and S. Goes (2007), Dynamic models of downgoing plate-buoyancy driven subduction: Subduction motions and energy dissipation, *Earth Planet. Sci. Lett.*, *262*(1–2), 284–297, doi:10.1016/j.epsl.2007.07.039.

Capitanio, F. A., G. Morra, and S. Goes (2009), Dynamics of plate bending at the trench and slab-plate coupling, *Geochem. Geophys. Geosyst.*, *10*, Q04002, doi:10.1029/2008GC002348.

Capitanio, F. A., D. R. Stegman, L. N. Moresi, and W. Sharples (2010), Upper plate controls on deep subduction, trench migrations and deformations at convergent margins, *Tectonophysics*, *483*(1–2), 80–92, doi:10.1016/j.tecto.2009.08.020.

Christensen, U. R., and D. A. Yuen (1984), The interaction of a subducting lithospheric slab with a chemical or phase boundary, *J. Geophys. Res.*, *89*(B6), 4389–4402, doi:10.1029/JB089iB06p04389.

Conrad, C. P., and B. H. Hager (1999), Effects of plate bending and fault strength at subduction zones on plate dynamics, *J. Geophys. Res.*, *104*, 17,551–17,571, doi:10.1029/1999JB900149.

Conrad, C. P., and B. H. Hager (2001), Mantle convection with strong subduction zones, *Geophys. J. Int.*, *144*(2), 271–288, doi:10.1046/j.1365-246x.2001.00321.x.

Conrad, C. P., and C. Lithgow-Bertelloni (2002), How mantle slabs drive plate tectonics, *Science*, *298*(5591), 207–209, doi:10.1126/science.1074161.

Di Giuseppe, E., J. van Hunen, F. Funiciello, C. Faccenna, and D. Giardini (2008), Slab stiffness control of trench motion: Insights from numerical models, *Geochem. Geophys. Geosyst.*, *9*, Q02014, doi:10.1029/2007GC001776.

Faccenna, C., P. Davy, J.-P. Brun, R. Funiciello, D. Giardini, M. Mattei, and T. Nalpas (1996), The dynamic of backarc basins: An experimental approach to the opening of the Tyrrhenian Sea, *Geophys. J. Int.*, *126*, 781–795, doi:10.1111/j.1365-246X.1996.tb04702.x.

Faccenna, C., T. W. Becker, F. P. Lucente, L. Jolivet, and F. Rossetti (2001), History of subduction and back-arc extension in the Central Mediterranean, *Geophys. J. Int.*, *145*(3), 809–820, doi:10.1046/j.0956-540x.2001.01435.x.

Forsyth, D., and S. Uyeda (1975), On the relative importance of the driving forces of plate motion, *Geophys. J. R. Astron. Soc.*, *43*, 163–200.

Forsyth, D. W., N. Harmon, D. S. Scheirer, and R. A. Duncan (2006), Distribution of recent volcanism and the morphology of seamounts and ridges in the GLIMPSE study area: Implications for the lithospheric cracking hypothesis for the origin of intraplate, non-hot spot volcanic chains, *J. Geophys. Res.*, *111*, B11407, doi:10.1029/2005JB004075.

Funiciello, F., C. Faccenna, D. Giardini, and K. Regenauer-Lieb (2003a), Dynamics of retreating slabs: 2. Insights from three-dimensional laboratory experiments, *J. Geophys. Res.*, *108*(B4), 2207, doi:10.1029/2001JB000896.

Funiciello, F., G. Morra, K. Regenauer-Lieb, and D. Giardini (2003b), Dynamics of retreating slabs: 1. Insights from two-dimensional numerical experiments, *J. Geophys. Res.*, *108*(B4), 2206, doi:10.1029/2001JB000898.

Gerya, T. V., J. A. D. Connolly, and D. A. Yuen (2008), Why is terrestrial subduction one-sided?, *Geology*, *36*(1), 43–46, doi:10.1130/G24060A.1.

Goes, S., F. A. Capitanio, and G. Morra (2008), Evidence of lower-mantle slab penetration phases in plate motions, *Nature*, *451*(7181), 981–984, doi:10.1038/nature06691.

Goes, S., F. A. Capitanio, G. Morra, M. Seton, and D. Giardini (2011), Signatures of downgoing plate-buoyancy driven subduction in Cenozoic plate motions, *Phys. Earth Planet. Inter.*, *184*(1–2), 1–13, doi:10.1016/j.pepi.2010.10.007.

Goodwillie, A. M., and B. Parsons (1992), Placing bounds on lithospheric deformation in the central Pacific Ocean, *Earth Planet. Sci. Lett.*, *111*(1), 123–139, doi:10.1016/0012-821X(92)90174-T.

Gurnis, M., M. Turner, S. Zahirovic, L. DiCaprio, S. Spasojevic, R. D. Müller, J. Boyden, M. Seton, V. C. Manea, and D. J. Bower (2012), Plate tectonic reconstructions with continuously closing plates, *Comput. Geosci.*, *38*, 35–42, doi:10.1016/j.cageo.2011.04.014.

Hager, B. H. (1984), Subducted slabs and the geoid: Constraints on mantle rheology and flow, *J. Geophys. Res.*, *89*(B7), 6003–6015, doi:10.1029/JB089iB07p06003.

Hager, B. H., and R. J. O'Connell (1981), A simple global model of plate dynamics and mantle convection, *J. Geophys. Res.*, *86*(B6), 4843–4867, doi:10.1029/JB086iB06p04843.

Han, L. J., and M. Gurnis (1999), How valid are dynamic models of subduction and convection when plate motions are prescribed?, *Phys. Earth Planet. Inter.*, *110*(3–4), 235–246, doi:10.1016/S0031-9201(98)00156-3.

Heuret, A., F. Funiciello, C. Faccenna, and S. Lallemand (2007), Plate kinematics, slab shape and back-arc stress: A comparison between laboratory models and current subduction zones, *Earth Planet. Sci. Lett.*, *256*(3–4), 473–483, doi:10.1016/j.epsl.2007.02.004.

Iaffaldano, G., H.-P. Bunge, and T. H. Dixon (2006), Feedback between mountain belt growth and plate convergence, *Geology*, *34*(10), 893–896, doi:10.1130/G22661.1.

Jadamec, M. A., and M. I. Billen (2010), Reconciling surface plate motions with rapid three-dimensional mantle flow around a slab edge, *Nature*, *465*(7296), 338–341, doi:10.1038/nature09053.

Jiménez-Munt, I., and J. P. Platt (2006), Influence of mantle dynamics on the topographic evolution of the Tibetan Plateau: Results from numerical modeling, *Tectonics*, *25*, TC6002, doi:10.1029/2006TC001963.

King, S. D. (2001), Subduction zones: Observations and geodynamic models, *Phys. Earth Planet. Inter.*, *127*(1–4), 9–24, doi:10.1016/S0031-9201(01)00218-7.

King, S. D., J. P. Lowman, and C. W. Gable (2002), Episodic tectonic plate reorganizations driven by mantle convection, *Earth Planet. Sci. Lett.*, *203*, 83–91, doi:10.1016/S0012-821X(02)00852-X.

Ladyzhenskaya, O. (1963), *The Mathematical Theory of Viscous Incompressible Flow*, 184 pp., Gordon and Breach, New York.

Lee, C.-K., S.-C. Han, and B. Steinberge (2010), Influence of variable uncertainties in seismic tomography models on constraining mantle viscosity from geoid observations, *Phys. Earth Planet. Inter.*, *184*(1–2), 51–62.

Lithgow-Bertelloni, C., and J. H. Guynn (2004), Origin of the lithospheric stress field, *J. Geophys. Res.*, *109*, B01408, doi:10.1029/2003JB002467.

Lithgow-Bertelloni, C., and M. Richards (1998), The dynamics of Cenozoic and Mesozoic plate motions, *Rev. Geophys.*, *36*, 27–78, doi:10.1029/97RG02282.

Loiselet, C., L. Husson, and J. Braun (2009), From longitudinal slab curvature to slab rheology, *Geology*, *37*(8), 747–750, doi:10.1130/G30052A.1.

Manga, M., and H. A. Stone (1995), Collective hydrodynamics of deformable drops and bubbles in dilute low Reynolds number suspensions, *J. Fluid Mech.*, *300*, 231–263, doi:10.1017/S0022112095003673.

Mitrovica, J. X. (1996), Haskell [1935] revisited, *J. Geophys. Res.*, *101*(B1), 555–569, doi:10.1029/95JB03208.

Mjelde, R., and J. Faleide (2009), Variation of Icelandic and Hawaiian magmatism: Evidence for co-pulsation of mantle plumes?, *Mar. Geophys. Res.*, *30*(1), 61–72, doi:10.1007/s11001-009-9066-0.

Moresi, L., and M. Gurnis (1996), Constraints on the lateral strength of slabs from three-dimensional dynamic flow models, *Earth Planet. Sci. Lett.*, *138*(1–4), 15–28, doi:10.1016/0012-821X(95)00221-W.

Morra, G., K. Regenauer-Lieb, and D. Giardini (2006), Curvature of oceanic arcs, *Geology*, *34*(10), 877–880, doi:10.1130/G22462.1.

Morra, G., P. Chatelain, P. Tackley, and P. Koumoutsakos (2007), Large scale three-dimensional boundary element simulation of subduction, in *Computational Science–ICCS 2007, Part III*, *Lect. Notes Comput. Sci.*, vol. 4489, pp. 1122–1129, Springer, Berlin.

Morra, G., P. Chatelain, P. Tackley, and P. Koumoutsakos (2009), Earth curvature effects on subduction morphology: Modeling subduction in a spherical setting, *Acta Geotech.*, *4*(2), 95–105, doi:10.1007/s11440-008-0060-5.

Morra, G., D. A. Yuen, L. Boschi, P. Chatelain, P. Koumoutsakos, and P. J. Tackley (2010), The fate of the slabs interacting with a density/viscosity hill in the mid-mantle, *Phys. Earth Planet. Inter.*, *180*, 271–282, doi:10.1016/j.pepi.2010.04.001.

Pozrikidis, C. (1992), *Boundary Integral and Singularity Methods for Linearized Viscous Flow*, Cambridge Univ. Press, New York, doi:10.1017/CBO9780511624124.

Pozrikidis, C. (2002), *Boundary Element Method*, Chapman and Hall, Boca Raton, Fla.

Rallison, J. M., and A. Acrivos (1978), A numerical study of the deformation and burst of a viscous drop in an extensional flow, *J. Fluid Mech.*, *89*(1), 191–200, doi:10.1017/S0022112078002530.

Regenauer-Lieb, K., D. A. Yuen, and J. Branlund (2001), The initiation of subduction: Criticality by addition of water?, *Science*, *294*, 578–580, doi:10.1126/science.1063891.

Regenauer-Lieb, K., B. Hobbs, D. A. Yuen, A. Ord, Y. Zhang, H. B. Mulhaus, and G. Morra (2006), From point defects to plate tectonic faults, *Philos. Mag.*, *86*, 3373–3392, doi:10.1080/14786430500375159.

Ribe, N. M. (2001), Bending and stretching if thin viscous sheets, *J. Fluid Mech.*, *433*, 135–160.

Ribe, N. M. (2010), Bending mechanics and mode selection in free subduction: A thin-sheet analysis, *Geophys. J. Int.*, *180*(2), 559–576, doi:10.1111/j.1365-246X.2009.04460.x.

Ricard, Y., and C. Vigny (1989), Mantle dynamics with induced plate tectonics, *J. Geophys. Res.*, *94*(B12), 17,543–17,559, doi:10.1029/JB094iB12p17543.

Ricard, Y., M. Richards, C. Lithgow-Bertelloni, and Y. Le Stunff (1993), A geodynamic model of mantle density heterogeneity, *J. Geophys. Res.*, *98*(B12), 21,895–21,909, doi:10.1029/93JB02216.

Saad, Y., and M. H. Schultz (1986), GMRES: A generalized minimal residual algorithm for solving nonsymmetric linear systems, *SIAM J. Sci. Stat. Comput.*, *7*(3), 856–869, doi:10.1137/0907058.

Salvadori, A. (2010), Analytical integrations in 3D BEM for elliptic problems: Evaluation and implementation, *Int. J. Numer. Methods Eng.*, *84*(5), 505–542.

Sammis, C. G., and Y. Ben-Zion (2008), Mechanics of grain-size reduction in fault zones, *J. Geophys. Res.*, *113*, B02306, doi:10.1029/2006JB004892.

Sandwell, D. T., E. L. Winterer, J. Mammerickx, R. A. Duncan, M. A. Lynch, D. A. Levitt, and C. L. Johnson (1995), Evidence for diffuse extension of the Pacific plate from Pukapuka ridges and cross-grain gravity lineations, *J. Geophys. Res.*, *100*(B8), 15,087–15,099, doi:10.1029/95JB00156.

Schellart, W. P. (2005), Influence of the subducting plate velocity on the geometry of the slab and migration of the subduction hinge, *Earth Planet. Sci. Lett.*, *231*, 197–219, doi:10.1016/j.epsl.2004.12.019.

Schellart, W. P., G. S. Lister, and M. W. Jessell (2002), Analogue modeling of arc and backarc deformation in the New Hebrides arc and North Fiji Basin, *Geology*, *30*(4), 311–314, doi:10.1130/0091-7613(2002)030<0311:AMOAAB>2.0.CO;2.

Schellart, W. P., J. Freeman, D. R. Stegman, L. Moresi, and D. May (2007), Evolution and diversity of subduction zones controlled by slab width, *Nature*, *446*, 308–311, doi:10.1038/nature05615.

Schellart, W. P., D. R. Stegman, and J. Freeman (2008), Global trench migration velocities and slab migration induced upper mantle volume fluxes: Constraints to find an Earth reference frame based on minimizing viscous dissipation, *Earth Sci. Rev.*, *88*(1–2), 118–144, doi:10.1016/j.earscirev.2008.01.005.

Schmeling, H., et al. (2008), A benchmark comparison of spontaneous subduction models–Towards a free surface, *Phys. Earth Planet. Inter.*, *171*(1–4), 198–223, doi:10.1016/j.pepi.2008.06.028.

Sdrolias, M., and R. D. Müller (2006), Controls on back-arc basin formation, *Geochem. Geophys. Geosyst.*, *7*, Q04016, doi:10.1029/2005GC001090.

Sornette, D., and V. Pisarenko (2003), Fractal plate tectonics, *Geophys. Res. Lett.*, *30*(3), 1105, doi:10.1029/2002GL015043.

Stadler, G., M. Gurnis, C. Burstedde, L. C. Wilcox, L. Alisic, and O. Ghattas (2010), The dynamics of plate tectonics and mantle flow: From local to global scales, *Science*, *329*(5995), 1033–1038, doi:10.1126/science.1191223.

Stegman, D. R., J. Freeman, W. P. Schellart, L. Moresi, and D. May (2006), Influence of trench width on subduction hinge retreat rates in 3-D models of slab rollback, *Geochem. Geophys. Geosyst.*, *7*, Q03012, doi:10.1029/2005GC001056.

Stegman, D. R., R. Farrington, F. A. Capitanio, and W. P. Schellart (2010a), A regime diagram for subduction styles from 3-D numerical models of free subduction, *Tectonophysics*, *483*(1–2), 29–45, doi:10.1016/j.tecto.2009.08.041.

Stegman, D. R., W. P. Schellart, and J. Freeman (2010b), Competing influences of plate width and far-field boundary conditions on trench migration and morphology of subducted slabs in the upper mantle, *Tectonophysics*, *483*(1–2), 46–57, doi:10.1016/j.tecto.2009.08.026.

Steinberger, B., R. Sutherland, and R. J. O'Connell (2004), Prediction of Emperor-Hawaii seamount locations from a revised model of global plate motion and mantle flow, *Nature*, *430*(6996), 167–173, doi:10.1038/nature02660.

Tackley, P. (2000a), Self-consistent generation of tectonic plates in time-dependent, three-dimensional mantle convection simulations. 2. Strain weakening and asthenosphere, *Geochem. Geophys. Geosyst.*, *1*(8), 1026, doi:10.1029/2000GC000043.

Tackley, P. (2000b), Self-consistent generation of tectonic plates in time-dependent, three-dimensional mantle convection simulations: 1. Pseudoplastic yielding, *Geochem. Geophys. Geosyst.*, *1*(8), 1021, doi:10.1029/2000GC000036.

Tan, E., E. Choi, P. Thoutireddy, M. Gurnis, and M. Aivazis (2006), GeoFramework: Coupling multiple models of mantle convection within a computational framework, *Geochem. Geophys. Geosyst.*, *7*, Q06001, doi:10.1029/2005GC001155.

Tarduno, J., H.-P. Bunge, N. Sleep, and U. Hansen (2009), The bent Hawaiian-Emperor hotspot track: Inheriting the mantle wind, *Science*, *324*(5923), 50–53, doi:10.1126/science.1161256.

Tornberg, A.-K., and L. Greengard (2008), A fast multipole method for the three-dimensional Stokes equations, *J. Comput. Phys.*, *227*(3), 1613–1619, doi:10.1016/j.jcp.2007.06.029.

Torsvik, T. H., B. Steinberger, L. R. M. Cocks, and K. Burke (2008), Longitude: Linking Earth's ancient surface to its deep interior, *Earth Planet. Sci. Lett.*, *276*(3–4), 273–282, doi:10.1016/j.epsl.2008.09.026.

Trompert, R., and U. Hansen (1998), Mantle convection simulations with rheologies that generate plate-like behaviour, *Nature*, *395*, 686–689, doi:10.1038/27185.

van der Meer, D. G., W. Spakman, D. J. J. van Hinsbergen, M. L. Amaru, and T. H. Torsvik (2010), Towards absolute plate motions constrained by lower-mantle slab remnants, *Nat. Geosci.*, *3*(1), 36–40, doi:10.1038/ngeo708.

van Dinther, Y., G. Morra, F. Funiciello, and C. Faccenna (2010), Role of the overriding plate in the subduction process: Insights from numerical models, *Tectonophysics*, *484*(1–4), 74–86, doi:10.1016/j.tecto.2009.08.038.

Veevers, J. J. (2000), Change of tectono-stratigraphic regime in the Australian plate during the 99 Ma (mid-Cretaceous) and 43 Ma (mid-Eocene) swerves of the Pacific, *Geology*, *28*(1), 47–50, doi:10.1130/0091-7613(2000)28<47:COTRIT>2.0.CO;2.

Wessel, P., Y. Harada, and L. W. Kroenke (2006), Toward a self-consistent, high-resolution absolute plate motion model for the Pacific, *Geochem. Geophys. Geosyst.*, *7*, Q03L12, doi:10.1029/2005GC001000.

Whittaker, J., R. D. Müller, G. Leitchenkov, H. Stagg, M. Sdrolias, C. Gaina, and A. Goncharov (2007), Major Australian-Antarctic plate reorganization at Hawaiian-Emperor bend time, *Science*, *318*, 83–86, doi:10.1126/science.1143769.

Wu, B., C. P. Conrad, A. Heuret, C. Lithgow-Bertelloni, and S. Lallemand (2008), Reconciling strong slab pull and weak plate bending: The plate motion constraint on the strength of mantle slabs, *Earth Planet. Sci. Lett.*, *272*(1–2), 412–421, doi:10.1016/j.epsl.2008.05.009.

Zhong, S., and M. Gurnis (1995a), Mantle convection with plates and mobile, faulted plate margins, *Science*, *267*, 838–843, doi:10.1126/science.267.5199.838.

Zhong, S., and M. Gurnis (1995b), Towards a realistic simulation of plate margins in mantle convection, *Geophys. Res. Lett.*, *22*, 981–984, doi:10.1029/95GL00782.

Zhong, S., M. T. Zuber, L. Moresi, and M. Gurnis (2000), Role of temperature-dependent viscosity and surface plates in spherical shell models of mantle convection, *J. Geophys. Res.*, *105*(B5), 11,063–11,082, doi:10.1029/2000JB900003.

Zhu, G., A. A. Mammoli, and H. Power (2006), A 3-D indirect boundary element method for bounded creeping flow of drops, *Eng. Anal. Boundary Elem.*, *30*, 856–868, doi:10.1016/j.enganabound.2006.07.002.